REYNOLDS AND FAVRE-AVERAGED RAPID DISTORTION THEORY FOR COMPRESSIBLE, IDEAL-GAS TURBULENCE

A Thesis

by

TUCKER ALAN LAVIN

Submitted to the Office of Graduate Studies of
Texas A&M University
in partial fulfillment of the requirements for the degree of

MASTER OF SCIENCE

May 2007

Major Subject: Aerospace Engineering

REYNOLDS AND FAVRE-AVERAGED RAPID DISTORTION THEORY FOR COMPRESSIBLE, IDEAL-GAS TURBULENCE

A Thesis

by

TUCKER ALAN LAVIN

Submitted to the Office of Graduate Studies of
Texas A&M University
in partial fulfillment of the requirements for the degree of

MASTER OF SCIENCE

Approved by:

Chair of Committee,	Sharath S. Girimaji
Committee Members,	Adonios Karpetis
	Hamn-Ching Chen
Head of Department,	Helen Reed

May 2007

Major Subject: Aerospace Engineering

ABSTRACT

Reynolds and Favre-Averaged Rapid Distortion Theory
for Compressible, Ideal-Gas Turbulence. (May 2007)
Tucker Alan Lavin, B.S., Texas A&M University
Chair of Advisory Committee: Dr. Sharath S. Girimaji

Compressible ideal-gas turbulence subjected to homogeneous shear is investigated at the rapid distortion limit. Specific issues addressed are (i) the interaction between kinetic and internal energies and role of pressure-dilatation; (ii) the modifications to pressure-strain correlation and Reynolds stress anisotropy and (iii) the effect of the composition of velocity fluctuations (solenoidal vs. dilatational). Turbulence evolution is found to be strongly influenced by gradient Mach number, the initial solenoidal-to-dilatational ratio of the velocity field and the initial intensity of the thermodynamic fluctuations. The balance between the initial fluctuations in velocity and thermodynamic variables is also found to be very important. Any imbalance in the two fluctuating fields leads to high levels of pressure-dilatation and intense exchange.

For a given initial condition, it is found that the interaction via the pressure-dilatation term between the momentum and energy equations reaches a peak at an intermediate gradient Mach number. The energy exchange between internal and kinetic modes is negligible at very high or very low Mach number values due to lack of pressure dilatation. When present, the exchange exhibits oscillations even as the sum of the two energies evolves smoothly. The interaction between shear and solenoidal initial velocity field generates dilatational fluctuations; for some intermediate levels of shear Mach number dilatational fluctuations account for 20% of the total fluctuations. Similarly, the interaction between shear and initial dilatation produces solenoidal os-

cillations. Somewhat surprisingly, the generation of solenoidal fluctuations increases with gradient Mach number. Larger levels of pressure-strain correlation are seen with dilatational rather than solenoidal initial conditions. Anisotropies of solenoidal and dilatational components are investigated individually. The most interesting observation is that solenoidal and dilatational turbulence tend toward a one componential state but the energetic component is different in each case. As in incompressible shear flows, with solenoidal fluctuations, the streamwise (1,1) component of Reynolds stress is dominant. With dilatational fluctuations, the stream-normal (2,2) component is the strongest. Overall, the study yields valuable insight into the linear processes in high Mach number shear flows and identifies important closure modeling issues.

To Rebecca

ACKNOWLEDGMENTS

I would like to thank my advisor and committee chair, Dr. Sharath S. Girimaji. His abilities as a skillful lecturer and wisdom as a mentor in the area of research are unmatched. He has made that which at first seemed academically unattainable and daunting a little more attainable (though still daunting).

I would also like to thank the other members of my committee Dr. Adonios Karpetis and Dr. Hamn-Ching Chen. Their abilities are stellar and stand out in a crowded and extremely challenging field.

A researcher is only so good as those on his research team. I owe a great deal to everyone on my research team, who helped me through the roadblocks and many twists and turns of research. Special thanks go to: Sawan Suman, Kurnchul Lee, Ben Riley, Sunny Jain and Dr. Huidan Yu. I also owe many thanks to my friends in graduate school who helped to make this time a bit more bearable; there are so many to thank, but I can only mention a few: Paul Gesting, Allen Parish, Julie Jones, Rick Rhodes, Brian Richardson, and Lesley Weitz.

My abilities were cemented early in my academic career due especially to two outstanding high school teachers: Mr. Nelson Bishop and Mr. Billy Talley. Mr. Bishop presented calculus to me so well that he made it seem easy, and I owe a great deal of my accolades in that field to him. Mr. Talley has been a wonderful choir teacher and mentor to me throughout my life; more than just music, he taught me the discipline to set and pursue goals, and to do so in a way that honors the Lord.

Obviously I could not have made it this far academically and in life without the supporting love of my family: my parents, Tom and Elise; my brother, Brian; and my grandparents, Bonnie and Bob. Most especially, thanks to my parents who sacrificed so greatly emotionally and financially to pave the way for my academic future. Their

example has given me a model to strive for with my own family, and their support has been invaluable in helping to make me the man I am today.

I am so grateful to Rebecca, my lovely bride-to-be, for enduring my long nights away at the lab so that I could finish this effort. She is such a precious gift from the Lord, and has been such a motivation to me in both the highs and the lows I've experienced during this time. To her parents, I am grateful for enduring my seemingly ever-constant presence at their house and for raising such a wonderful daughter in Rebecca.

The Lord has given me the mental capacity to understand (or at least faintly grasp) what it is that I have been studying these past several years. Not only that, Christ has given me a reason and joy to strive to use these gifts as best suits His glory and man's needs. Above everything else, all thanks and honor for any good I am able to do in life ultimately should and must go to Him.

TABLE OF CONTENTS

Page

LIST OF FIGURES

FIGURE Page

FIGURE Page

FIGURE Page

FIGURE Page

FIGURE Page

LIST OF TABLES

CHAPTER I

INTRODUCTION

The inherent complexity of turbulence is further compounded in compressible flows by the dynamic coupling between flow and thermodynamic variables. In incompressible flows, pressure is merely a Lagrange multiplier with the sole function of imposing the divergence-free constraint. The evolution of incompressible turbulence is governed entirely by the momentum conservation equation subject to the kinematic incompressibility constraint. However, in compressible flows the momentum and energy conservation equations are tightly linked via the equations of state and the dependence of transport coefficients on thermodynamic variables. Thus, velocity field fluctuations are tightly coupled with those of pressure, temperature, and density. As in the case of any compressible flow, compressible turbulence can be classified into different types based on the applicable state equation. Possible categories of compressible turbulence classification, in order of increasing complexity, are: (i) isothermal; (ii) isentropic; (iii) ideal gas and (iv) real gas. In barotropic flows (isothermal and isentropic), pressure is a direct function of density and the energy equation is redundant. Such flows are perhaps too elementary for many practical applications that motivate this work. At the other extreme, turbulent flows under the influence of real gas effects, while practically relevant, do not easily lend themselves to fundamental investigation. In this work we will consider ideal gas compressible turbulence, which is of intermediate degree of complexity and yet of great utility. The extent of flow-thermodynamics coupling, given a state equation, depends upon factors such as Mach number, type of mean-velocity gradient, intensity of thermodynamic fluctuations, etc. Naturally, the

---

This thesis follows the journal style of *IEEE Transactions on Automatic Control*.

coupling is weak at low Mach numbers and can be expected to be more significant at higher Mach numbers. The goal of this study is to investigate the effect of large homogeneous shear on compressible ideal gas turbulence over a wide range of Mach numbers and thermodynamic conditions.

In ideal-gas compressible turbulence, flow-thermodynamics coupling leads to active exchange of energy between kinetic and internal (i.e. thermal) modes via the pressure work or pressure-dilatation. Unlike viscous work, which leads to unidirectional energy transfer from kinetic to internal form, pressure-dilatation transfer can be in both directions. The two-way energy interchange renders the various turbulence processes such as pressure-redistribution and spectral cascade more complicated than in incompressible flows. One of the central goals of this study is to examine the energy interchange between the turbulent kinetic energy and mean internal energy.

A. Rapid Distortion Theory

Inviscid rapid distortion theory (RDT) [1] is a computationally and analytically viable option for examining linear compressible flow physics in the absence of cascade and viscous effects. As the rapid pressure-strain term plays an important role in the evolution of turbulence [2], a better understanding of this term is sought. Insofar as incompressible flows are concerned, RDT has provided valuable insight into the rapid pressure-strain redistribution process which has led to important improvements in closure modeling (see reviews by [3, 4] and references therein). In particular, RDT has played a significant role in improving our understanding of the effects of system rotation [5], stratification [6] and mean-flow unsteadiness [7] on turbulence. Analysis of compressible flows using RDT has been more recent.

The application of RDT to compressible turbulence is rendered more complex as

the homogeneity condition requires mean thermodynamic properties like density and temperature to be spatially invariant, in addition to the mean velocity gradient being uniform in space. Further, the restriction to isentropic flows has been deemed necessary in the past to close the set of governing equations, without the detailed consideration of the thermodynamics of the flow. Subject to these limitations, homogeneous turbulence RDT of compressible flows has been performed [5, 8, 9, 10, 11, 12, 13]. The effect of anisotropic mean strains have been studied at low turbulent Mach numbers [8]. Initial degree of compressibility and its effects on kinetic energy evolution have also been examined [12]. A more thorough review of the work performed to date in RDT of compressible homogeneous turbulence is given in Yu & Girimaji [14].

While these studies have been useful in providing better insight into compressible turbulence physics, the incorporation of more realistic thermodynamic properties is needed to make further progress. The first step in that direction has been taken [15], wherein ideal gas compressible turbulence subject to rapid shear is investigated. But the approach in [15] is limited to homogeneous shear and the study does not address the flow-thermodynamics coupling.

Yu & Girimaji [14] develop the formalism required to extend RDT of ideal-gas compressible turbulence to all mean velocity gradients. Mass, momentum and energy conservation equations along with the ideal gas equation of state are employed. This approach allows for the investigation of flow-thermodynamics coupling.

B. Focus of Current Work

The objective of this work is to study the effect of rapid homogeneous shear on ideal-gas compressible turbulence using the RDT equations developed in [14]. While there are many important issues, this thesis will focus on three key aspects not addressed

in previous studies: (i) the interaction between kinetic and internal energies and the role of pressure-dilatation; (ii) the effect of initial composition of velocity fluctuations (solenoidal vs. dilatational) and (iii) compressibility effects on pressure-strain correlation and Reynolds stress anisotropy.

It is apparent from the equations that pressure-dilatation is the link between the kinetic and internal modes in compressible flows. Examination of the evolution of pressure-dilatation reveals that the coupling of the momentum and energy equations is the strongest at an intermediate gradient Mach number, at which shear and acoustic timescales are of the same order. In mechanical terms, pressure-dilatation is akin to a valve regulating the flow of energy between internal and kinetic modes. It is found that pressure-dilatation decreases to zero at very high or very low Mach numbers, and consequently energy ceases to be transferred to or from the internal mode. Naturally, the internal energy enhancement is proportional to the level of pressure-dilatation in the flow.

In all simulations, the ratio of solenoidal to dilatational kinetic energy reaches a constant value at asymptotic state. The amount of energy in the solenoidal mode for initially-solenoidal turbulence at this asymptotic state is approximately 80%; by comparison, for initially-dilatational turbulence, the amount of energy in the solenoidal mode is much less. Initially dilatational turbulence remains dilatational at low gradient Mach numbers. It is not until higher levels of shear are applied that energy is more likely to be transferred to the solenoidal mode, before falling again at some later time. It is also found that the gradient Mach number which produces maximum pressure-dilatation (and, thus, maximum temperature growth) coincides with the gradient Mach number for which the amount of kinetic energy residing in the dilatational mode is the highest. It stands to reason then that temperature growth is higher for the initially-dilatational turbulence than for the initially-solenoidal turbulence.

Given adequate time, the internal energy growth rate also attains a steady value; thus, a relationship can be found between the initial compressibility in the flow, the gradient Mach number and the amount of energy transferred to the internal mode. The anisotropies, when divided into solenoidal and dilatational components, reveal that the solenoidal portion of the flow is more or less unaffected by the amount of compressibility in the initial conditions (and, thus, by the influence of pressure-dilatation). On the other hand, the dilatational portion of the flow is profoundly affected. Additionally, the solenoidal portion of the flow is found to be dominant in the streamwise (1,1) direction, while the dilatational fluctuations are predominantly in the stream-normal (2,2) direction.

The remainder of the thesis is organized as follows. Chapter II briefly discusses the governing equations and compressible second-moment Reynolds-averaged rapid distortion theory (R-RDT) and discusses the numerical implementation. The results for R-RDT are presented in Chapter III. The Favre-averaged rapid distortion theory (F-RDT) derivation and implementation is discussed in Chapter IV, with its results presented in Chapter V. Finally, Chapter VI provides a summary discussion and concludes the thesis.

CHAPTER II

RAPID DISTORTION THEORY: REYNOLDS-AVERAGED STATISTICS

In this chapter, we discuss salient features of the derivation of the Reynolds-averaged RDT equations (R-RDT), and also discuss briefly the numerical implementation of the equations.

A. Methodology

The derivation of the inviscid R-RDT equations follows that performed in [14]. The governing equations are the Euler conservation equations for compressible flow and the state equation of an ideal gas.

$$\frac{\partial \rho}{\partial t} + U_j \frac{\partial \rho}{\partial x_j} = -\rho \frac{\partial U_j}{\partial x_j}, \tag{2.1a}$$

$$\frac{\partial U_i}{\partial t} + U_j \frac{\partial U_i}{\partial x_j} = -\frac{1}{\rho}\frac{\partial P}{\partial x_i}, \tag{2.1b}$$

$$\frac{\partial T}{\partial t} + U_j \frac{\partial T}{\partial x_j} = -(\gamma - 1) T \frac{\partial U_j}{\partial x_j} \tag{2.1c}$$

$$P = \rho R T \tag{2.1d}$$

where γ is the ratio of specific heats.

The instantaneous values of velocity, density, temperature and pressure in the governing equations are partitioned using a Reynolds decomposition into mean and fluctuating parts: $U_i = \overline{U}_i + u_i^{'}$, $\rho = \overline{\rho} + \rho^{'}$, $T = \overline{T} + T^{'}$ and $P = \overline{P} + P^{'}$. The resulting system of equations can be written as:

$$\frac{\partial(\overline{\rho} + \rho^{'})}{\partial t} + (\overline{U}_j + u_j^{'}) \frac{\partial(\overline{\rho} + \rho^{'})}{\partial x_j} = -(\overline{\rho} + \rho^{'}) \frac{\partial(\overline{U}_j + u_j^{'})}{\partial x_j}, \tag{2.2a}$$

$$\frac{\partial(\overline{U}_i + u_i^{'})}{\partial t} + (\overline{U}_j + u_j^{'})\frac{\partial(\overline{U}_i + u_i^{'})}{\partial x_j} = -\frac{1}{(\overline{\rho} + \rho^{'})}\frac{\partial(\overline{P} + P^{'})}{\partial x_i}, \tag{2.2b}$$

$$\frac{\partial(\overline{T} + T^{'})}{\partial t} + (\overline{U}_j + u_j^{'})\frac{\partial(\overline{T} + T^{'})}{\partial x_j} = -(\gamma - 1)(\overline{T} + T^{'})\frac{\partial(\overline{U}_j + u_j^{'})}{\partial x_j}, \tag{2.2c}$$

$$\overline{P} + P^{'} = R\overline{\rho}\overline{T} + R\overline{\rho}T^{'} + R\rho^{'}\overline{T} + R\rho^{'}T^{'}. \tag{2.2d}$$

The density in the denominator on the righthand side of Eq. (2.2b) can be written using a Taylor series expansion as follows:

$$\frac{1}{(\overline{\rho} + \rho^{'})} = \frac{1}{\overline{\rho}} - \frac{\rho^{'}}{(\overline{\rho})^2} + \frac{(\rho^{'})^2}{(\overline{\rho})^3} - \cdots . \tag{2.3}$$

Taking the mean of Eq. (2.2) yields the following equations:

$$\frac{\partial\overline{\rho}}{\partial t} + \overline{U}_j\frac{\partial\overline{\rho}}{\partial x_j} = -\overline{\rho}\frac{\partial\overline{U}_j}{\partial x_j} - \frac{\partial\overline{\rho^{'}u_j^{'}}}{\partial x_j}, \tag{2.4a}$$

$$\frac{\partial\overline{U}_i}{\partial t} + \overline{U}_j\frac{\partial\overline{U}_i}{\partial x_j} + \overline{u_j^{'}\frac{\partial u_i^{'}}{\partial x_j}} = -\frac{1}{\overline{\rho}}\frac{\partial\overline{P}}{\partial x_i} + \frac{1}{\overline{\rho}^2}\overline{\rho^{'}\frac{\partial P^{'}}{\partial x_i}} - \frac{\overline{(\rho^{'})^2}}{(\overline{\rho})^3}\frac{\partial\overline{P}}{\partial x_i} + \cdots , \tag{2.4b}$$

$$\frac{\partial\overline{T}}{\partial t} + \overline{U}_j\frac{\partial\overline{T}}{\partial x_j} + \overline{u_j^{'}\frac{\partial T^{'}}{\partial x_j}} = -(\gamma - 1)\overline{T}\frac{\partial\overline{U}_j}{\partial x_j} - (\gamma - 1)\overline{T^{'}\frac{\partial u_j^{'}}{\partial x_j}}, \tag{2.4c}$$

$$\overline{P} = R\overline{\rho}\overline{T} + R\overline{\rho^{'}T^{'}}. \tag{2.4d}$$

As in the case of incompressible RDT, we will consider all terms of order three or higher in fluctuations as negligible. Thus we seek Reynolds-averaged first (mean) and second-order statistics equations accurate to second order in fluctuations.

Next, the mean of the equations are subtracted from Eq. 2.2 to obtain the fluctuating flow equations. Subtracting Eq. (2.4a) from Eq. (2.2a) gives:

$$\frac{\partial \rho^{'}}{\partial t} + \overline{U}_k \frac{\partial \rho^{'}}{\partial x_k} = - u_k^{'} \frac{\partial \overline{\rho}}{\partial x_k} - u_k^{'} \frac{\partial \rho^{'}}{\partial x_k} + \overline{u_k^{'} \frac{\partial \rho^{'}}{\partial x_k}} - \overline{\rho} \frac{\partial u_k^{'}}{\partial x_k} - \rho^{'} \frac{\partial \overline{U}_k}{\partial x_k} - \rho^{'} \frac{\partial u_k^{'}}{\partial x_k} + \overline{\rho^{'} \frac{\partial u_k^{'}}{\partial x_k}}. \tag{2.5}$$

Subtracting Eq. (2.4b) from Eq. (2.2b) gives:

$$\frac{\partial u_i^{'}}{\partial t} + \overline{U}_k \frac{\partial u_i^{'}}{\partial x_k} = - u_k^{'} \frac{\partial \overline{U}_i}{\partial x_k} - u_k^{'} \frac{\partial u_i^{'}}{\partial x_k} + \overline{u_k^{'} \frac{\partial u_i^{'}}{\partial x_k}} - \frac{1}{\overline{\rho}} \frac{\partial P^{'}}{\partial x_i} + \frac{\rho^{'}}{(\overline{\rho})^2} \frac{\partial \overline{P}}{\partial x_i} + \frac{\rho^{'}}{(\overline{\rho})^2} \frac{\partial P^{'}}{\partial x_i} - \frac{(\rho^{'})^2}{(\overline{\rho})^3} \frac{\partial \overline{P}}{\partial x_i} - \frac{1}{\overline{\rho}^2} \overline{\rho^{'} \frac{\partial P^{'}}{\partial x_i}} + \frac{\overline{(\rho^{'})^2}}{(\overline{\rho})^3} \frac{\partial \overline{P}}{\partial x_i}. \tag{2.6}$$

However, subtracting Eq. (2.4d) from Eq. (2.2d) gives the fluctuating pressure equation:

$$P^{'} = R\overline{\rho} T^{'} + R\rho^{'} \overline{T} + R\rho^{'} T^{'} - R\overline{\rho^{'} T^{'}} \tag{2.7}$$

which can be substituted into Eq. 2.6 to give:

$$\begin{aligned} \frac{\partial u_i^{'}}{\partial t} + \overline{U}_k \frac{\partial u_i^{'}}{\partial x_k} = & - u_k^{'} \frac{\partial \overline{U}_i}{\partial x_k} - u_k^{'} \frac{\partial u_i^{'}}{\partial x_k} + \overline{u_k^{'} \frac{\partial u_i^{'}}{\partial x_k}} + \frac{\rho^{'}}{(\overline{\rho})^2} \frac{\partial \overline{P}}{\partial x_i} \\ & - \frac{(\rho^{'})^2}{(\overline{\rho})^3} \frac{\partial \overline{P}}{\partial x_i} + \frac{\overline{(\rho^{'})^2}}{(\overline{\rho})^3} \frac{\partial \overline{P}}{\partial x_i} \\ & - \frac{R}{\overline{\rho}^2} \overline{\rho^{'} \left(\frac{\partial (\overline{\rho} T^{'})}{\partial x_i} + \frac{\partial (\rho^{'} \overline{T})}{\partial x_i} \right)} \\ & - \frac{R}{\overline{\rho}} \frac{\partial}{\partial x_i} (\overline{\rho} T^{'} + \rho^{'} \overline{T} + \rho^{'} T^{'} - \overline{\rho^{'} T^{'}}) \\ & + \frac{R\rho^{'}}{(\overline{\rho})^2} \frac{\partial}{\partial x_i} (\overline{\rho} T^{'} + \rho^{'} \overline{T}). \end{aligned} \tag{2.8}$$

Finally, subtracting Eq. (2.4c) from Eq. (2.2c) gives:

$$\frac{\partial T^{'}}{\partial t}+\overline{U}_k\frac{\partial T^{'}}{\partial x_k}=-u_k^{'}\frac{\partial \overline{T}}{\partial x_k}-u_k^{'}\frac{\partial T^{'}}{\partial x_k}+\overline{u_k^{'}\frac{\partial T^{'}}{\partial x_k}}-(\gamma-1)\overline{T}\frac{\partial u_k^{'}}{\partial x_k}$$
$$-(\gamma-1)T^{'}\frac{\partial \overline{U}_k}{\partial x_k}-(\gamma-1)T^{'}\frac{\partial u_k^{'}}{\partial x_k}+(\gamma-1)\overline{T^{'}\frac{\partial u_k^{'}}{\partial x_k}}. \tag{2.9}$$

B. Homogeneity Assumptions

It must be stressed that the above equations are general for inviscid compressible turbulence with the state equation of ideal gas. The only assumption that has been made so far is that third and higher-order fluctuating moments are negligibly small and have thus been dropped from the equations. At this state, we will restrict our considerations to homogeneous turbulence. In compressible flow, the homogeneity condition requires that all moments involving velocity and thermodynamic fluctuations must be independent of spatial location:

$$\frac{\partial}{\partial x_i}\overline{\phi^{'}\phi^{'}}=\frac{\partial}{\partial x_i}\overline{\phi^{'}\phi^{'}\phi^{'}}=\cdots=0. \tag{2.10}$$

The necessary outcome of this is that all mean thermodynamic properties must also be invariant in space [14]:

$$\frac{\partial \overline{P}}{\partial x_k}=\frac{\partial \overline{\rho}}{\partial x_k}=\frac{\partial \overline{T}}{\partial x_k}=0 \tag{2.11}$$

As in incompressible turbulence, the mean velocity gradient must also be constant in space:

$$\frac{\partial \overline{U}_i}{\partial x_j}(\vec{x},t)=\frac{\partial \overline{U}_i}{\partial x_j}(t) \tag{2.12}$$

Thus the rapid distortion equations for fluctuating fields become:

$$\frac{d\rho^{'}}{dt} = -\frac{\partial(u_k^{'}\rho^{'})}{\partial x_k} - \overline{\rho}\frac{\partial u_k^{'}}{\partial x_k} - \rho^{'}\frac{\partial \overline{U}_k}{\partial x_k}, \tag{2.13a}$$

$$\begin{aligned}\frac{du_i^{'}}{dt} =& -u_k^{'}\frac{\partial \overline{U}_i}{\partial x_k} - u_k^{'}\frac{\partial u_i^{'}}{\partial x_k} + \overline{u_k^{'}\frac{\partial u_i^{'}}{\partial x_k}} - \frac{R}{\overline{\rho}}\overline{\rho^{'}\frac{\partial T^{'}}{\partial x_i}} \\ & - R\frac{\partial T^{'}}{\partial x_i} - \frac{R\overline{T}}{\overline{\rho}}\frac{\partial \rho^{'}}{\partial x_i} - \frac{RT^{'}}{\overline{\rho}}\frac{\partial \rho^{'}}{\partial x_i} + \frac{R\overline{T}\rho^{'}}{(\overline{\rho})^2}\frac{\partial \rho^{'}}{\partial x_i},\end{aligned} \tag{2.13b}$$

$$\begin{aligned}\frac{dT^{'}}{dt} =& -u_k^{'}\frac{\partial T^{'}}{\partial x_k} + \overline{u_k^{'}\frac{\partial T^{'}}{\partial x_k}} - (\gamma-1)\overline{T}\frac{\partial u_k^{'}}{\partial x_k} - (\gamma-1)T^{'}\frac{\partial \overline{U}_k}{\partial x_k} \\ & - (\gamma-1)T^{'}\frac{\partial u_k^{'}}{\partial x_k} + (\gamma-1)\overline{T^{'}\frac{\partial u_k^{'}}{\partial x_k}}.\end{aligned} \tag{2.13c}$$

With these simplified equations, we can construct second order moments of the fluctuating flow quantities:

$$\begin{aligned}\frac{d(u_i^{'}u_j^{'})}{dt} =& -u_j^{'}u_k^{'}\frac{\partial \overline{U}_i}{\partial x_k} - u_j^{'}u_k^{'}\frac{\partial u_i^{'}}{\partial x_k} + u_j^{'}\overline{u_k^{'}\frac{\partial u_i^{'}}{\partial x_k}} - \frac{Ru_j^{'}}{\overline{\rho}}\overline{\rho^{'}\frac{\partial T^{'}}{\partial x_i}} \\ & - Ru_j^{'}\frac{\partial T^{'}}{\partial x_i} - \frac{R\overline{T}u_j^{'}}{\overline{\rho}}\frac{\partial \rho^{'}}{\partial x_i} - \frac{RT^{'}u_j^{'}}{\overline{\rho}}\frac{\partial \rho^{'}}{\partial x_i} + \frac{R\overline{T}\rho^{'}u_j^{'}}{(\overline{\rho})^2}\frac{\partial \rho^{'}}{\partial x_i} \\ & - u_i^{'}u_k^{'}\frac{\partial \overline{U}_j}{\partial x_k} - u_i^{'}u_k^{'}\frac{\partial u_j^{'}}{\partial x_k} + u_i^{'}\overline{u_k^{'}\frac{\partial u_j^{'}}{\partial x_k}} - \frac{Ru_i^{'}}{\overline{\rho}}\overline{\rho^{'}\frac{\partial T^{'}}{\partial x_j}} \\ & - Ru_i^{'}\frac{\partial T^{'}}{\partial x_j} - \frac{R\overline{T}u_i^{'}}{\overline{\rho}}\frac{\partial \rho^{'}}{\partial x_j} - \frac{RT^{'}u_i^{'}}{\overline{\rho}}\frac{\partial \rho^{'}}{\partial x_j} + \frac{R\overline{T}\rho^{'}u_i^{'}}{(\overline{\rho})^2}\frac{\partial \rho^{'}}{\partial x_j}\end{aligned} \tag{2.14a}$$

$$\begin{aligned}\frac{d(u_i^{'}T^{'})}{dt} =& - T^{'}u_k^{'}\frac{\partial\overline{U}_i}{\partial x_k} - T^{'}u_k^{'}\frac{\partial u_i^{'}}{\partial x_k} + T^{'}\overline{u_k^{'}\frac{\partial u_i^{'}}{\partial x_k}} - \frac{RT^{'}}{\overline{\rho}}\overline{\rho^{'}\frac{\partial T^{'}}{\partial x_i}} \\ & - RT^{'}\frac{\partial T^{'}}{\partial x_i} - \frac{R\overline{T}T^{'}}{\overline{\rho}}\frac{\partial\rho^{'}}{\partial x_i} - \frac{R(T^{'})^2}{\overline{\rho}}\frac{\partial\rho^{'}}{\partial x_i} + \frac{R\overline{T}\rho^{'}T^{'}}{(\overline{\rho})^2}\frac{\partial\rho^{'}}{\partial x_i} \\ & - u_i^{'}u_k^{'}\frac{\partial T^{'}}{\partial x_k} + \overline{u_i^{'}u_k^{'}\frac{\partial T^{'}}{\partial x_k}} - (\gamma-1)\overline{T}u_i^{'}\frac{\partial u_k^{'}}{\partial x_k} \\ & - (\gamma-1)T^{'}u_i^{'}\frac{\partial\overline{U}_k}{\partial x_k} - (\gamma-1)T^{'}u_i^{'}\frac{\partial u_k^{'}}{\partial x_k} + (\gamma-1)\overline{u_i^{'}T^{'}\frac{\partial u_k^{'}}{\partial x_k}} \end{aligned} \tag{2.14b}$$

$$\begin{aligned}\frac{d(u_i^{'}\rho^{'})}{dt} =& - \rho^{'}u_k^{'}\frac{\partial\overline{U}_i}{\partial x_k} - \rho^{'}u_k^{'}\frac{\partial u_i^{'}}{\partial x_k} + \rho^{'}\overline{u_k^{'}\frac{\partial u_i^{'}}{\partial x_k}} - \frac{R\rho^{'}}{\overline{\rho}}\overline{\rho^{'}\frac{\partial T^{'}}{\partial x_i}} \\ & - R\rho^{'}\frac{\partial T^{'}}{\partial x_i} - \frac{R\overline{T}\rho^{'}}{\overline{\rho}}\frac{\partial\rho^{'}}{\partial x_i} - \frac{RT^{'}\rho^{'}}{\overline{\rho}}\frac{\partial\rho^{'}}{\partial x_i} + \frac{R\overline{T}(\rho^{'})^2}{(\overline{\rho})^2}\frac{\partial\rho^{'}}{\partial x_i} \\ & - u_i^{'}\frac{\partial(u_k^{'}\rho^{'})}{\partial x_k} - \overline{\rho}u_i^{'}\frac{\partial u_k^{'}}{\partial x_k} - \rho^{'}u_i^{'}\frac{\partial\overline{U}_k}{\partial x_k} \end{aligned} \tag{2.14c}$$

$$\begin{aligned}\frac{d(\rho^{'}T^{'})}{dt} =& - T^{'}\frac{\partial(u_k^{'}\rho^{'})}{\partial x_k} - \overline{\rho}T^{'}\frac{\partial u_k^{'}}{\partial x_k} - \rho^{'}T^{'}\frac{\partial\overline{U}_k}{\partial x_k} - \rho^{'}u_k^{'}\frac{\partial T^{'}}{\partial x_k} \\ & + \rho^{'}\overline{u_k^{'}\frac{\partial T^{'}}{\partial x_k}} - (\gamma-1)\overline{T}\rho^{'}\frac{\partial u_k^{'}}{\partial x_k} - (\gamma-1)\rho^{'}T^{'}\frac{\partial\overline{U}_k}{\partial x_k} \\ & - (\gamma-1)\rho^{'}T^{'}\frac{\partial u_k^{'}}{\partial x_k} + (\gamma-1)\rho^{'}\overline{T^{'}\frac{\partial u_k^{'}}{\partial x_k}} \end{aligned} \tag{2.14d}$$

$$\frac{d(\rho^{'}\rho^{'})}{dt} = 2\rho^{'}[-\frac{\partial(u_k^{'}\rho^{'})}{\partial x_k} - \overline{\rho}\frac{\partial u_k^{'}}{\partial x_k} - \rho^{'}\frac{\partial\overline{U}_k}{\partial x_k}] \tag{2.14e}$$

$$\begin{aligned}\frac{d(T^{'}T^{'})}{dt} =& 2T^{'}[-u_k^{'}\frac{\partial T^{'}}{\partial x_k} + \overline{u_k^{'}\frac{\partial T^{'}}{\partial x_k}} - (\gamma-1)\overline{T}\frac{\partial u_k^{'}}{\partial x_k} - (\gamma-1)T^{'}\frac{\partial\overline{U}_k}{\partial x_k} \\ & - (\gamma-1)T^{'}\frac{\partial u_k^{'}}{\partial x_k} + (\gamma-1)\overline{T^{'}\frac{\partial u_k^{'}}{\partial x_k}}] \end{aligned} \tag{2.14f}$$

Averaging Eq. (2.14) and invoking the assumption of homogeneous turbulence, the following moment equations are obtained:

$$\frac{d(\overline{u_i' u_j'})}{dt} = -\overline{u_j' u_k'}\frac{\partial \overline{U}_i}{\partial x_k} - \overline{u_i' u_k'}\frac{\partial \overline{U}_j}{\partial x_k} - R\overline{u_j'\frac{\partial T'}{\partial x_i}} - \frac{R\overline{T}}{\overline{\rho}}\overline{u_j'\frac{\partial \rho'}{\partial x_i}}$$
$$- R\overline{u_i'\frac{\partial T'}{\partial x_j}} - \frac{R\overline{T}}{\overline{\rho}}\overline{u_i'\frac{\partial \rho'}{\partial x_j}} - \overline{u_j' u_k'\frac{\partial u_i'}{\partial x_k}} - \overline{u_i' u_k'\frac{\partial u_j'}{\partial x_k}}$$
$$- \frac{R}{\overline{\rho}}\overline{T' u_j'\frac{\partial \rho'}{\partial x_i}} + \frac{R\overline{T}}{(\overline{\rho})^2}\overline{\rho' u_j'\frac{\partial \rho'}{\partial x_i}} - \frac{R}{\overline{\rho}}\overline{T' u_i'\frac{\partial \rho'}{\partial x_j}} + \frac{R\overline{T}}{(\overline{\rho})^2}\overline{\rho' u_i'\frac{\partial \rho'}{\partial x_j}} \tag{2.15a}$$

$$\frac{d(\overline{u_i' T'})}{dt} = -\overline{T' u_k'}\frac{\partial \overline{U}_i}{\partial x_k} - \frac{R\overline{T}}{\overline{\rho}}\overline{T'\frac{\partial \rho'}{\partial x_i}} - (\gamma-1)\overline{T} u_i'\overline{\frac{\partial u_k'}{\partial x_k}} - (\gamma-1)\overline{T' u_i'}\frac{\partial \overline{U}_k}{\partial x_k}$$
$$- \overline{T' u_k'\frac{\partial u_i'}{\partial x_k}} - \frac{R}{\overline{\rho}}\overline{(T')^2\frac{\partial \rho'}{\partial x_i}} + \frac{R\overline{T}}{(\overline{\rho})^2}\overline{\rho' T'\frac{\partial \rho'}{\partial x_i}} - \overline{u_i' u_k'\frac{\partial T'}{\partial x_k}}$$
$$- (\gamma-1)\overline{T' u_i'\frac{\partial u_k'}{\partial x_k}} \tag{2.15b}$$

$$\frac{d(\overline{u_i' \rho'})}{dt} = -\overline{\rho' u_k'}\frac{\partial \overline{U}_i}{\partial x_k} - R\overline{\rho'\frac{\partial T'}{\partial x_i}} - \overline{\rho} u_i'\overline{\frac{\partial u_k'}{\partial x_k}} - \overline{\rho' u_i'}\frac{\partial \overline{U}_k}{\partial x_k} - \frac{R}{\overline{\rho}}\overline{T'\rho'\frac{\partial \rho'}{\partial x_i}} \tag{2.15c}$$

$$\frac{d(\overline{\rho' T'})}{dt} = -\overline{\rho}\overline{T'\frac{\partial u_k'}{\partial x_k}} - \gamma\overline{\rho' T'}\frac{\partial \overline{U}_k}{\partial x_k} - (\gamma-1)\overline{T}\overline{\rho'\frac{\partial u_k'}{\partial x_k}} - (\gamma-1)\overline{\rho' T'\frac{\partial u_k'}{\partial x_k}} \tag{2.15d}$$

$$\frac{d(\overline{\rho'\rho'})}{dt} = -2\overline{\rho}\overline{\rho'\frac{\partial u_k'}{\partial x_k}} - 2\overline{\rho'\rho'}\frac{\partial \overline{U}_k}{\partial x_k} - 2\overline{\rho'\frac{\partial(u_k'\rho')}{\partial x_k}} \tag{2.15e}$$

$$\frac{d(\overline{T'T'})}{dt} = -2(\gamma-1)\overline{T}\overline{T'\frac{\partial u_k'}{\partial x_k}} - 2(\gamma-1)\overline{T'T'}\frac{\partial \overline{U}_k}{\partial x_k} - 2(\gamma-1.5)\overline{T'T'\frac{\partial u_k'}{\partial x_k}} \tag{2.15f}$$

As mentioned earlier, our objective is to solve the mean and second-order statistics equations accurate to second-order in fluctuations. Thus all third-order statistics will be omitted from further considerations from Eq. (2.15). Rather than solve the moment equations directly, we will solve the fluctuation equations in Fourier space,

as in traditional RDT [2].

Consistent with omitting third-order terms in second-moment equations, we consider only terms linear in fluctuations in the fluctuation evolution equations:

$$\frac{d\rho'}{dt} = -\overline{\rho}\frac{\partial u_k'}{\partial x_k} - \rho'\frac{\partial \overline{U}_k}{\partial x_k} \tag{2.16a}$$

$$\frac{du_i'}{dt} = -u_k'\frac{\partial \overline{U}_i}{\partial x_k} - R\frac{\partial T'}{\partial x_i} - \frac{R\overline{T}}{\overline{\rho}}\frac{\partial \rho'}{\partial x_i} \tag{2.16b}$$

$$\frac{dT'}{dt} = -(\gamma-1)\overline{T}\frac{\partial u_k'}{\partial x_k} - (\gamma-1)T'\frac{\partial \overline{U}_k}{\partial x_k} \tag{2.16c}$$

The linearity permits the use of superposition of results, which is key in Fourier RDT computations. The fluctuating variables are written in terms of their Fourier components:

$$\vec{u}'(\vec{x},t) = \sum_{\vec{\kappa}} \widehat{\vec{u}}(t)e^{i\vec{\kappa}(t)\cdot\vec{x}}, \quad \rho'(\vec{x},t) = \sum_{\vec{\kappa}} \widehat{\rho}(t)e^{i\vec{\kappa}(t)\cdot\vec{x}}, \quad T'(\vec{x},t) = \sum_{\vec{\kappa}} \widehat{T}(t)e^{i\vec{\kappa}(t)\cdot\vec{x}} \tag{2.17}$$

where $\vec{\kappa}(t)$ is the wavenumber vector and $\widehat{\vec{u}}$, $\widehat{\rho}$, and $\widehat{T}$ are the Fourier coefficients of the velocity, density, and temperature fluctuations, respectively. Eqs. (2.16) are then transformed to the following simpler ordinary differential equations (ODEs):

$$\frac{d\widehat{\rho}}{dt} = -i\overline{\rho}\kappa_k\widehat{u}_k - \frac{\partial \overline{U}_k}{\partial x_k}\widehat{\rho}, \tag{2.18a}$$

$$\frac{d\widehat{u}_i}{dt} = -\widehat{u}_k\frac{\partial \overline{U}_i}{\partial x_k} - i(R\widehat{T} + \frac{R\overline{T}}{\overline{\rho}}\widehat{\rho})\kappa_i, \tag{2.18b}$$

$$\frac{d\widehat{T}}{dt} = -i(\gamma-1)\overline{T}\kappa_k\widehat{u}_k - (\gamma-1)\frac{\partial \overline{U}_k}{\partial x_k}\widehat{T}, \tag{2.18c}$$

where i is the imaginary unit equal to $\sqrt{-1}$. The wavenumber vector evolves as [2]:

$$\frac{d\kappa_i}{dt} + \kappa_k \frac{\partial \overline{U}_k}{\partial x_i} = 0. \tag{2.19}$$

Eqs. (2.18) and (2.19) can be directly solved and then used to construct the required covariances of fluctuating terms. Instead, we follow an alternate approach recommended by Kassinos & Reynolds [16]. We define conditional moments given a wavenumber, as follows [2]:

$$\widehat{R}_{ij} \equiv \langle \widehat{u}_i^* \widehat{u}_j | \vec{\kappa} \rangle, \tag{2.20a}$$

$$\widehat{L}_j \equiv \langle \widehat{T}^* \widehat{u}_j | \vec{\kappa} \rangle, \tag{2.20b}$$

$$\widehat{M}_j \equiv \langle \widehat{\rho}^* \widehat{u}_j | \vec{\kappa} \rangle, \tag{2.20c}$$

$$\widehat{A} \equiv \langle \widehat{\rho}^* \widehat{T} | \vec{\kappa} \rangle, \tag{2.20d}$$

$$\widehat{B} \equiv \langle \widehat{T}^* \widehat{T} | \vec{\kappa} \rangle, \tag{2.20e}$$

$$\widehat{C} \equiv \langle \widehat{\rho}^* \widehat{\rho} | \vec{\kappa} \rangle. \tag{2.20f}$$

The evolution equations for the above conditional moments (i.e. covariances) of two Fourier coefficients can be derived from Eqs. (2.18) and (2.19):

$$\frac{d\widehat{R}_{ij}}{dt} = -\frac{\partial \overline{U}_i}{\partial x_k}\widehat{R}_{kj} - \frac{\partial \overline{U}_j}{\partial x_k}\widehat{R}_{ik} + iR(\widehat{L}_j\kappa_i - \widehat{L}_i^*\kappa_j) + i\frac{R\overline{T}}{\overline{\rho}}(\widehat{M}_j\kappa_i - \widehat{M}_i^*\kappa_j), \tag{2.21a}$$

$$\frac{d\widehat{M}_i}{dt} = i\overline{\rho}\kappa_k\widehat{R}_{ki} - \frac{\partial \overline{U}_k}{\partial x_k}\widehat{M}_i - \frac{\partial \overline{U}_i}{\partial x_k}\widehat{M}_k - iR\widehat{A}\kappa_i - i\frac{R\overline{T}}{\overline{\rho}}\widehat{C}\kappa_i, \tag{2.21b}$$

$$\frac{d\widehat{L}_i}{dt} = i(\gamma-1)\overline{T}\kappa_k\widehat{R}_{ki} - (\gamma-1)\frac{\partial \overline{U}_k}{\partial x_k}\widehat{L}_i - \frac{\partial \overline{U}_i}{\partial x_k}\widehat{L}_k - iR\widehat{B}\kappa_i - i\frac{R\overline{T}}{\overline{\rho}}\widehat{A}^*\kappa_i, \tag{2.21c}$$

$$\frac{d\widehat{A}}{dt} = i\overline{\rho}\kappa_k\widehat{L}_k^* - i(\gamma-1)\overline{T}\widehat{M}_k\kappa_k - \gamma\frac{\partial \overline{U}_k}{\partial x_k}\widehat{A}, \tag{2.21d}$$

$$\frac{d\widehat{B}}{dt} = -2(\gamma-1)\frac{\partial \overline{U}_k}{\partial x_k}\widehat{B} + i(\gamma-1)\overline{T}\kappa_k(\widehat{L}_k^* - \widehat{L}_k), \tag{2.21e}$$

$$\frac{d\widehat{C}}{dt} = -2\frac{\partial \overline{U}_k}{\partial x_k}\widehat{C} + i\overline{\rho}\kappa_k(\widehat{M}_k^* - \widehat{M}_k). \tag{2.21f}$$

We opt to solve Eq. (2.21) for the conditional covariance and obtain the various physical-space second-order moments by summing the terms over all wavenumbers using the following relation:

$$\overline{u_i u_j} = \sum_{\vec{\kappa}} \widehat{R}_{ij}(\vec{\kappa}, t), \tag{2.22a}$$

$$\overline{u_i T} = \sum_{\vec{\kappa}} \widehat{L}_i(\vec{\kappa}, t), \tag{2.22b}$$

$$\overline{\rho u_i} = \sum_{\vec{\kappa}} \widehat{M}_i(\vec{\kappa}, t), \tag{2.22c}$$

$$\overline{\rho T} = \sum_{\vec{\kappa}} \widehat{A}(\vec{\kappa}, t), \tag{2.22d}$$

$$\overline{T^2} = \sum_{\vec{\kappa}} \widehat{B}(\vec{\kappa}, t), \tag{2.22e}$$

$$\overline{\rho^2} = \sum_{\vec{\kappa}} \widehat{C}(\vec{\kappa}, t). \tag{2.22f}$$

This approach of solving for the conditional moments directly, rather than for the individual wavenumber amplitudes, has two very important advantages: (i) the statistical sampling error is significantly reduced as is the computational requirements [16], and (ii) the interdependence of various moments becomes immediately clear (e.g. it is clear that solving for all equations is necessary to obtain the Reynolds stresses). This insight is useful for closure modeling. Taking into account that each covariance consists of a real part and an imaginary part, Eqs. (2.19) and (2.21) include 26 independent ordinary differential equations (ODEs). A fourth-order Runge-Kutta

scheme [14] is used to solve these 26 ODEs in this thesis.

C. Numerical Implementation

The R-RDT equations are valid for arbitrary initial fields. As a preliminary step, we will focus on isotropic turbulence. While many different types of mean flow deformation are of interest, we consider steady homogeneous shear as defined by:

$$\frac{\partial \overline{U}_i}{\partial x_j} = \begin{pmatrix} 0 & S & 0 \\ 0 & 0 & 0 \\ 0 & 0 & 0 \end{pmatrix} \tag{2.23}$$

Initial conditions for the wavenumber vector and 25 covariances are specified in Fourier space. We first consider fully incompressible isotropic turbulence at $t = 0$. The wavenumber-vector $\vec{\kappa}(t = 0)$ and corresponding velocity covariance $R_{ij}(t = 0)$ are specified in the same way as by [17]; 6079 wavevectors are distributed about a unit sphere in Fourier space to render a statistically isotropic initial field. To ensure initial incompressibility, velocity vectors for each wavevector are chosen such that they are normal to the respective wavevector. For dilatational initial conditions, the amplitude and wavevectors are parallel. Density is set so that $\overline{\rho} = 1.0$, while initial mean temperature is set to 300°K. Finally, the correlation of density and temperature fluctuations are specified as percentages of the mean density (8%) and temperature (0.01%), respectively.

Based on previous studies [18], we recognize a gradient Mach number, M_g, as the relevant parameter:

$$M_g \equiv \frac{Sl}{\sqrt{\gamma R T_0}} \tag{2.24}$$

where R is the universal gas constant and T_0 is the initial temperature, and the initial characteristic length scale l is taken to be unity ($l = 1$).

As a validation of this method of specifying Mach number, it is important to note that the incompressible results by [2] are recovered at low values of S (i.e. $M_g = 0.01$) and the Burgers (i.e. high-Mach) limit is recovered at large values of S (i.e. $M_g = 2880$). The subject of this thesis will be the study of the flow physics at interim values of M_g.

D. Time-Step and Fourier Node Convergence Study

First, we perform a Fourier-node sensitivity study, carrying out computations with three sets of Fourier nodes: 4006, 6079 and 12001. Care is taken to ensure that initial conditions (e.g. incompressibility, isotropy, kinetic and internal energy, etc.) are consistent across all three cases. Figs. 1 and 2 show kinetic energy and internal energy fraction plots (to be discussed in more detail later), respectively, for the three different gradient Mach number cases: $M_g = 0.01$ (incompressible limit), $M_g = 1.00$ and $M_g = 2880$ (Burgers limit). Excellent agreement is achieved in all three cases. Based on the results, 6079 wavevectors are appropriate to be used in this study.

Convergence in time-step size must also be demonstrated. The time-step sizes specified in Table I are used in the study. Simulations are performed for the standard time-step size used in this study and half of that time-step size. Plots of kinetic energy and internal energy fraction for the same three values of M_g are shown in Figs. 3 and 4, respectively. The results are practically identical for all three values of M_g for both quantities considered. Throughout this work, we use the time-step sizes specified as case 1 in Table I.

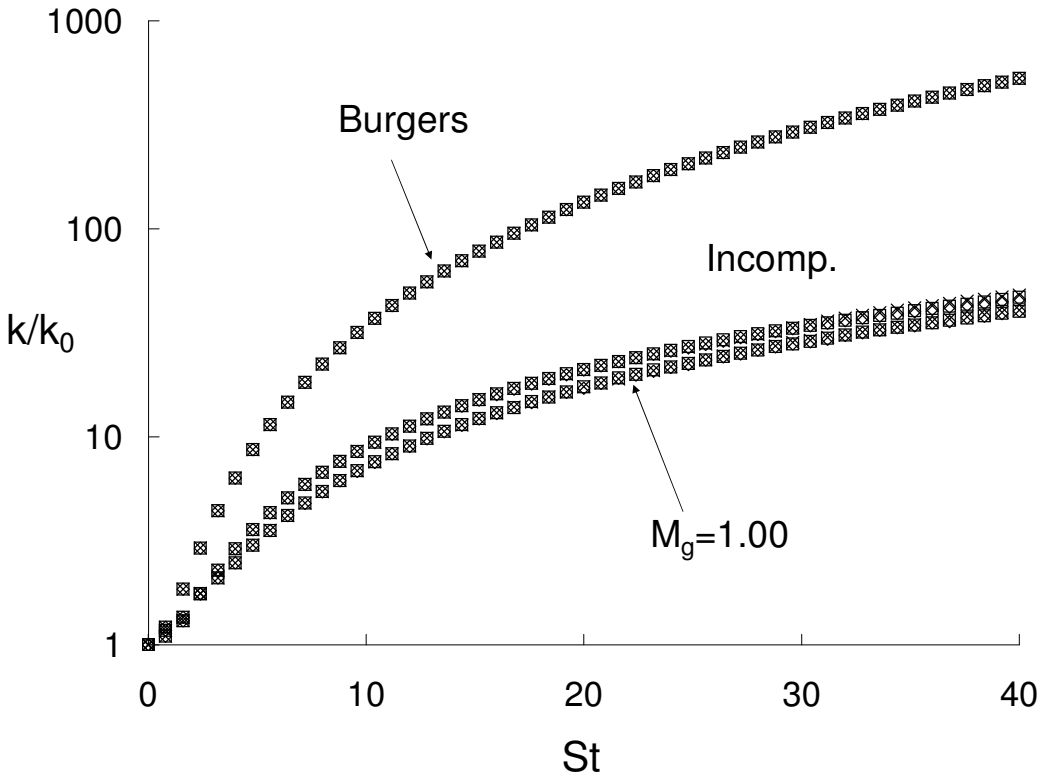

Fig. 1. R-RDT kinetic energy growth at coarse, medium and fine resolution in Fourier space for the incompressible limit, $M_g = 1.00$ and Burgers limit cases. Symbols represent - $\Diamond$: coarse resolution (4006 wavenumbers); $\Box$: medium resolution (6079 wavenumbers); $\times$: fine resolution (12001 wavenumbers)

Table I. Time-step sizes used in convergence study

M_g range	$\triangle t$ (case 1)	$\triangle t$ (case 2)
0.01	0.00004	0.00002
0.29-0.72	0.0001	0.00005
> 1.0	0.001	0.0005

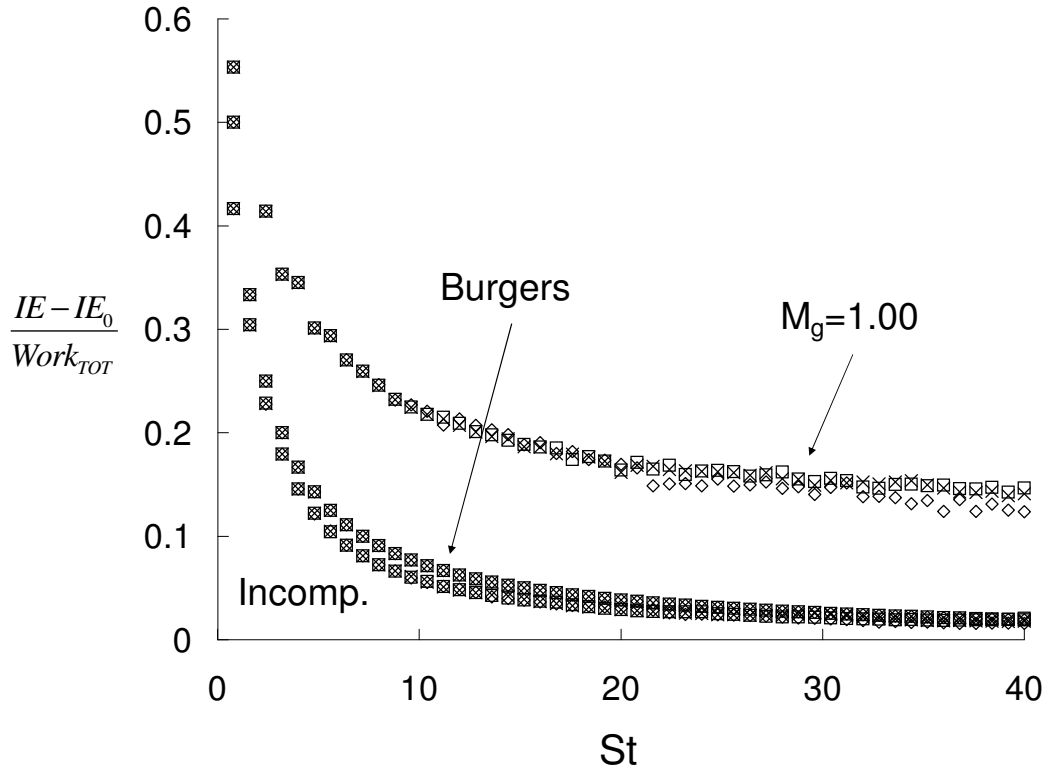

Fig. 2. R-RDT internal energy growth as a fraction of total work produced by shear at coarse, medium and fine resolution in Fourier space for the incompressible limit, $M_g = 1.00$ and Burgers limit cases. Symbols represent - ◊: coarse resolution (4006 wavenumbers); □: medium resolution (6079 wavenumbers); ×: fine resolution (12001 wavenumbers)

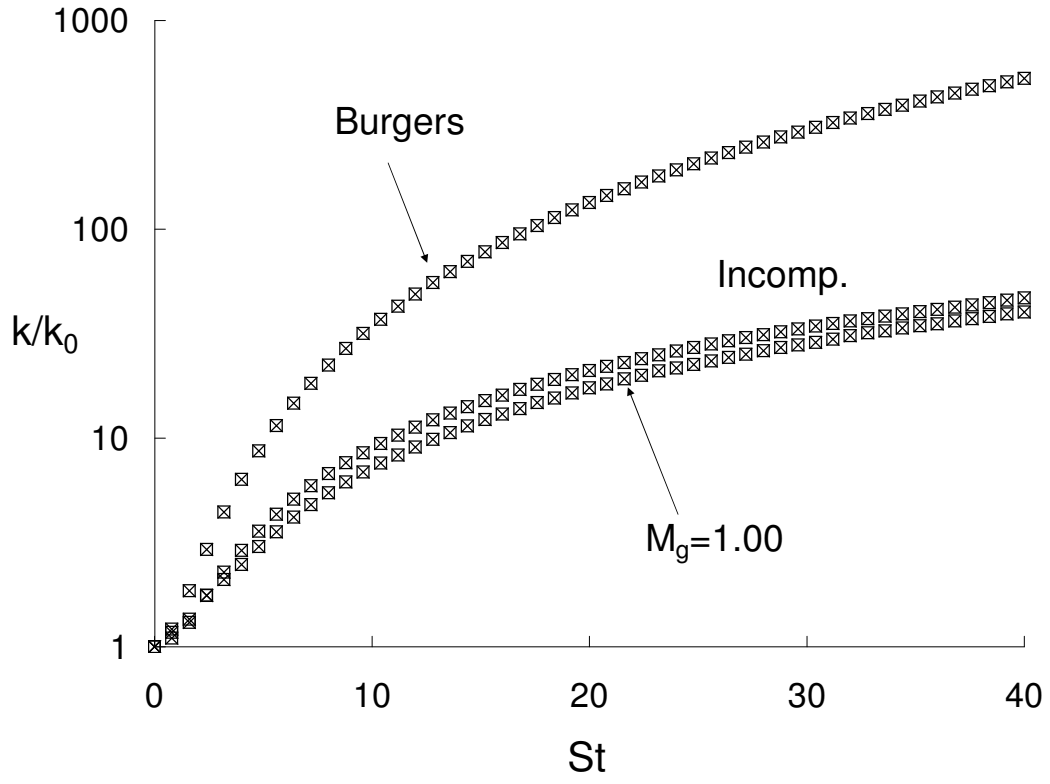

Fig. 3. R-RDT kinetic energy growth at regular and half time-steps for the incompressible limit, $M_g = 1.00$ and Burgers limit cases. Symbols represent - $\boxtimes$: regular time-step; $\times$: double time-step

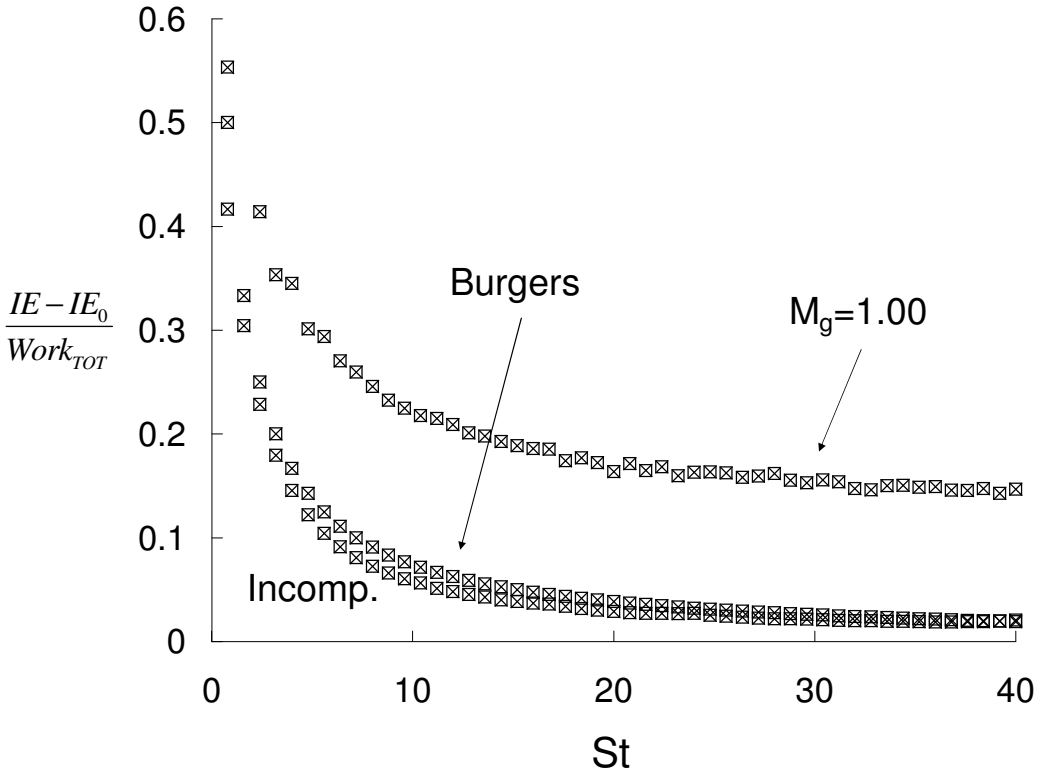

Fig. 4. R-RDT internal energy growth at regular and half time-steps for the incompressible limit, $M_g = 1.00$ and Burgers limit cases. Symbols represent - □: regular time-step; ×: double time-step

CHAPTER III

R-RDT RESULTS

It has already been shown [14] that the R-RDT equations perform very well at the incompressible and Burgers limits for homogeneous shear. Now we extend R-RDT to interim shear values between the two limits. This section contains the results stemming from R-RDT calculations for a variety of different initial conditions over a large range of gradient Mach numbers (M_g).

A. Evolution of Kinetic Energy

While the behavior of kinetic energy growth is well-documented at the upper (i.e. high-Mach) and lower limit (i.e. incompressible regime) of flows in RDT, not much is known of the interim region with these given initial conditions and taking into consideration the thermal influences on the flow. Normalized kinetic energy evolution for R-RDT is plotted for various mean shear values from $M_g = 0.01$ (incompressible limit) to $M_g = 2880$ (Burgers limit) in Fig. 5.

Several trends can be noted from the plot of turbulent kinetic energy growth. There seems to be three distinct behaviors of the interim values of mean shear. Initially, the evolution typically follows the pressure-released trend (i.e. $M_g = 2880$) before peeling off in an oscillatory manner and then following the incompressible trend (i.e. $M_g = 0.01$), though falling below that curve for a couple cases. As $St \to \infty$, it seems that the kinetic energy settles at decreasing magnitudes as gradient Mach number increases. This is counterintuitive, since it seems that shearing the flow more rapidly should lead to a larger amount of kinetic energy in the flow; however, a similar trend is found by [13]. It turns out that this phenomenon is a consequence of observing the results in shear-time St (in which the results of more-highly sheared

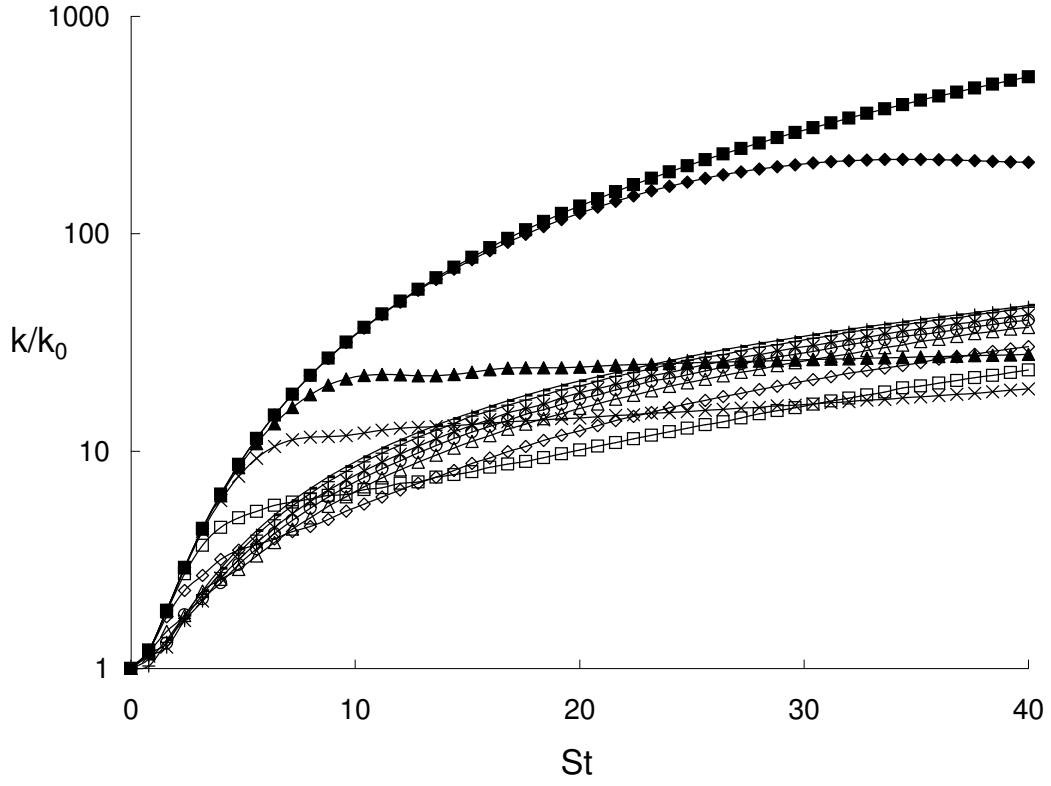

Fig. 5. The evolution of normalized turbulent kinetic energy with solenoidal initial conditions. Plotted for a range of gradient Mach numbers M_g: −: 0.01; +: 0.29; ∗: 0.72; ∘:1.00; △: 1.44; ◇: 2.88; □: 5.76; ×: 14.4; ▲: 28.8; ♦: 288; ■: 2880.

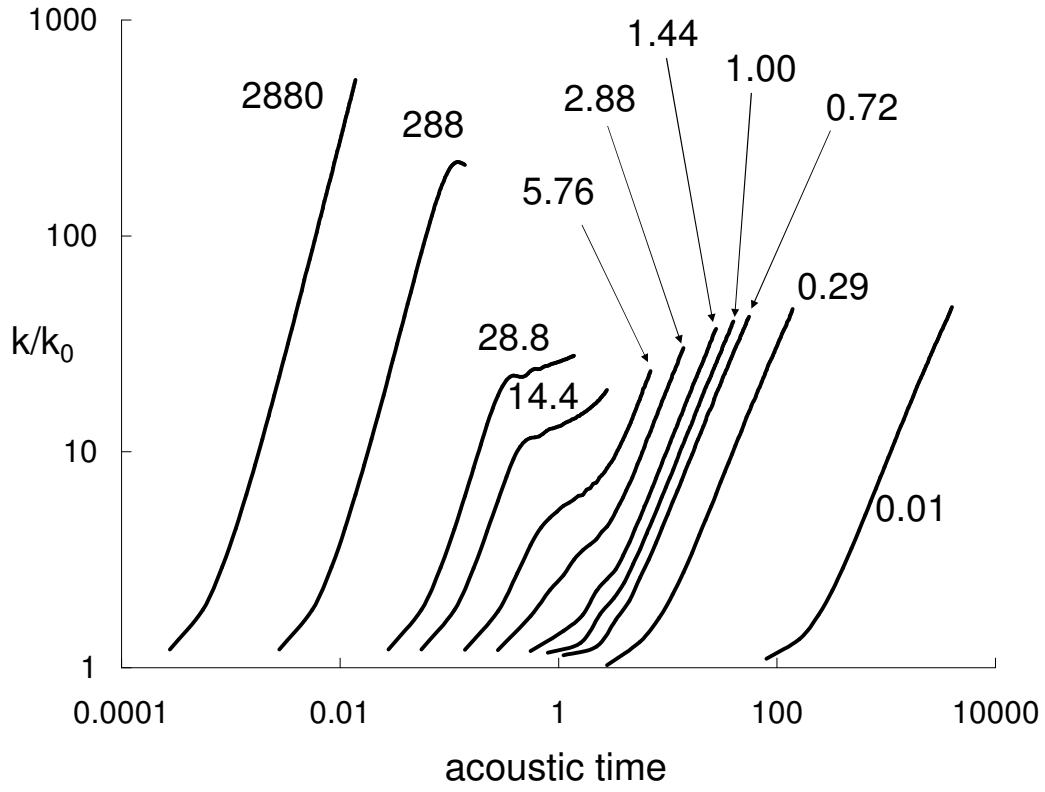

Fig. 6. Kinetic energy evolution scaled with acoustic time with solenoidal initial conditions at various specified gradient Mach numbers.

flows are stretched) as opposed to real time. If time is scaled according to an acoustic timescale (i.e. $t\sqrt{\gamma RT_0}$), as shown in Fig. 6, it can be seen that the kinetic energy decreases monotonically as gradient Mach number is decreased.

Fig. 6 also reveals that, though we have made observations of the behavior of more highly-sheared flows near the Burgers limit in shear-time, the actual effects that we observe occur very quickly in acoustic time; while the physical applications of these observations of highly-sheared flows may be few, these highly-sheared flows can still add to our understanding of the physics of the R-RDT equations.

B. Role of Pressure-Dilatation

The goal of this thesis is to develop insight into the role of pressure-dilatation (represented as $\langle pd \rangle$) for the purpose of developing improved closure models.

1. Oscillatory Nature of Pressure

Wavelike properties are seen in the interim gradient Mach numbers in Fig. 5 which are eventually suppressed as the shear is further increased. Closer examination reveals that these oscillations are a result of pressure - i.e. the last two terms on the right side of Eq. (2.21a) which stem from the pressure gradient term in Eq. (2.4b). As mean shear S is increased, the first two terms of this equation dominate over the remaining terms and minimize the effect of pressure terms at early times. This explains why the onset of oscillations is suppressed as gradient Mach number increases. However, given enough time, the wave-like trend eventually influences the kinetic energy growth, even for the case where $M_g = 2880$, as can be seen in Fig. 7 when compared to the Burgers (i.e. pressure-released) limit. It can be seen from this figure that oscillations still develop for the case where $M_g = 2880$ and the curve eventually reverts to a lower exponential curve.

This phenomenon can be explained by realizing that these pressure terms, while being independent shear directly, are proportional to $\overline{\kappa}(t)$. In homogeneous shear flows, the only component of the wavevector that grows with time is given by [2]:

$$\widehat{\kappa}_2(t) = -(\widehat{\kappa}_1)_0 St + (\widehat{\kappa}_2)_0 \tag{3.1}$$

where the subscript 0 indicates initial values. Therefore, whatever the chosen value of shear (or M_g), the influence of the pressure terms will grow with time. The choice of gradient Mach number, however, determines how long in shear-time it will take

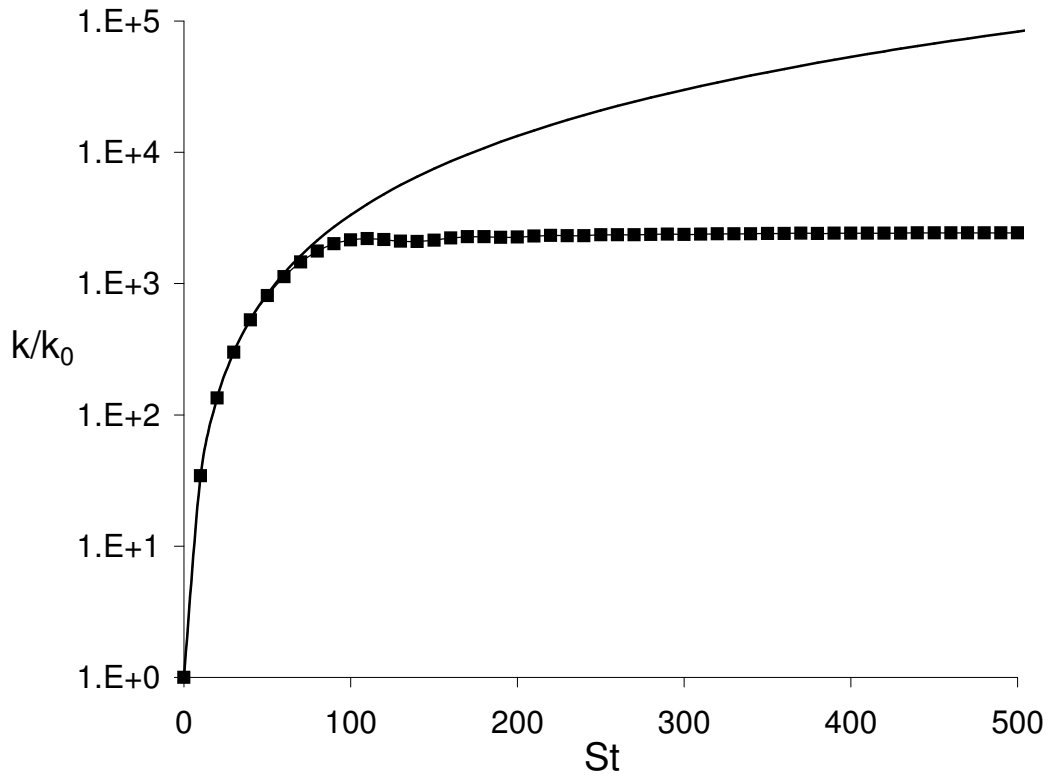

Fig. 7. The evolution of high-shear kinetic energy with developing oscillations at long St. Symbols represent - solid line: pressure-released limit; ■: $M_g = 2880$.

for this onset of wave-like behavior to occur. The oscillations that develop over time should come as no surprise, as pressure is inherently wave-like in nature. As shear is increased, the timescale of the flow decreases relative to the timescale of pressure; thus, more time is required to allow the influence of pressure to be felt by the flow.

2. Pathological Behavior

From Fig. 5, there appears to be a difference in trends between the lower and higher gradient Mach number flows. It was initially thought that this pathological switch in trend is a result of the physics first spending energy to make the flow compressible before the energy could be absorbed into other energy modes at later times. To test the validity of this premise, the kinetic energy is divided into solenoidal and dilatational components (i.e. into components of energy projected onto the plane normal to $\widehat{\kappa}_3$ and onto $\widehat{\kappa}_3$ itself, respectively). The growth of solenoidal and dilatational components of kinetic energy for the initially incompressible and compressible cases can be found in Fig. 8.

From this figure, it can be seen that the fraction of kinetic energy at time $St = 0$ can be seen as purely solenoidal (i.e. incompressible), which is expected as we began with fully solenoidal initial conditions. Also as can be expected, the kinetic energy remains completely solenoidal at the incompressible limit ($M_g = 0.01$), with incompressible initial conditions. Of interest in this figure is that the kinetic energy fraction remains mostly in the solenoidal mode; the solenoidal percentage for the $M_g = 0.72 - 1.44$ range is about 80% from about the beginning of the simulation, while other gradient Mach numbers tend toward 80% as time progresses. Other behavior that is apparent from Fig. 8 is that the shear component of the equations tends to drive the kinetic energy back to incompressibility. However, as pressure is given time to act, oscillations develop and return some compressibility to the flow (in

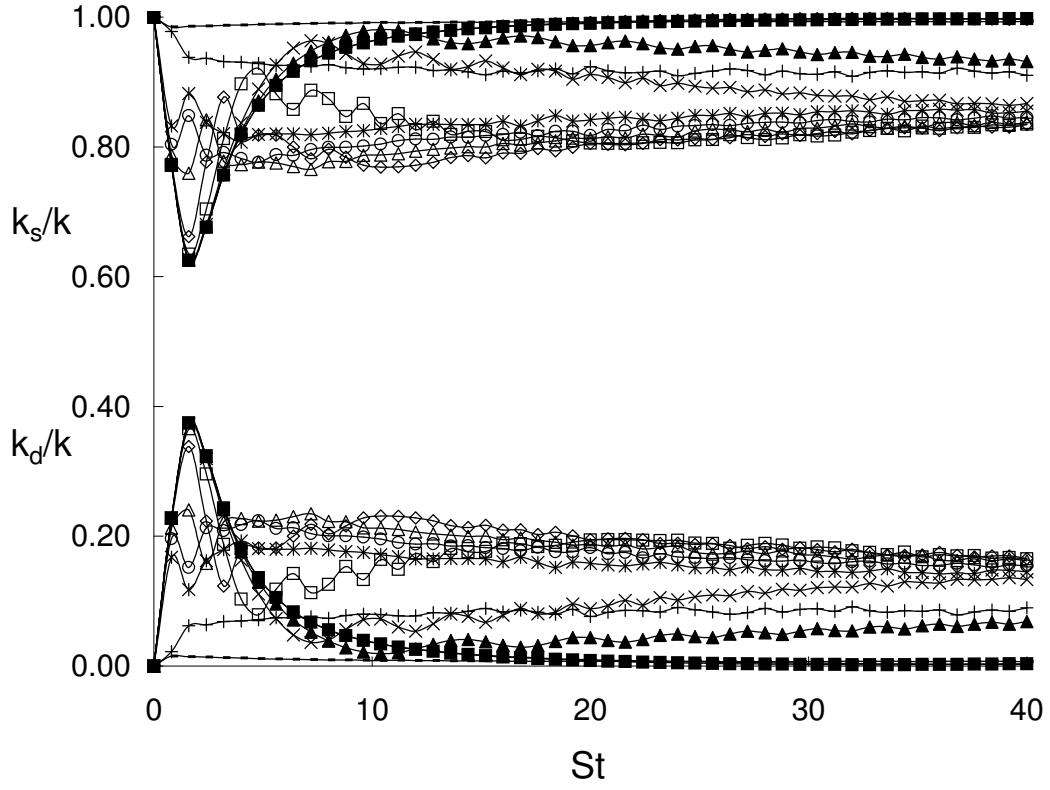

Fig. 8. Normalized solenoidal (k_s/k) and dilatational (k_d/k) kinetic energy plots with solenoidal initial conditions. Plotted for a range of gradient Mach numbers M_g: $-$: 0.01; $+$: 0.29; $*$: 0.72; $\circ$:1.00; $\triangle$: 1.44; $\Diamond$: 2.88; $\square$: 5.76; $\times$: 14.4; $\blacktriangle$: 28.8; $\blacklozenge$: 288; $\blacksquare$: 2880.

the high-Mach case where pressure is negligible, kinetic energy reverts back entirely to the solenoidal mode); note also that the occurrence of these oscillations is delayed as M_g is increased. It seems that, as the total amount of kinetic energy present in the flow continues to increase with time (as the constantly-applied shear continues to do work on the flow), the division of the kinetic energy between solenoidal and dilatational components eventually reaches a constant (80% and 20%, respectively), independent of gradient Mach number.

As a check to ensure proper calculation of the solenoidal and dilatational kinetic energy components, the cross-components of kinetic energy (i.e. that portion of energy composed of both solenoidal and dilatational kinetic energy - $\overline{u_1^d u_1^s}$, $\overline{u_2^d u_2^s}$ and $\overline{u_3^d u_3^s}$) were calculated for both solenoidal and dilatational initial conditions. The results of this computation are plotted in Fig. 9; the values are found to be negligibly small, as expected.

3. Energy Balance of Kinetic and Internal Modes

The fluctuations observed in kinetic energy growth caused by the pressure terms motivate the examination of the mechanisms behind energy transfer in the R-RDT equations. Since no energy is being inserted into the flow except for the work done by production via the applied mean shear, the only other energy present is that at the initial state. The energy balance can best be described with the evolution equations of Reynolds-averaged kinetic energy and Favre-averaged mean temperature:

$$\overline{\rho}\frac{\partial}{\partial t}\left(\frac{\overline{u_i u_i}}{2}\right) + \overline{\rho}\frac{\partial \overline{U_i}}{\partial x_j}\overline{u_i u_j} = \overline{p'\frac{\partial u_i'}{x_j}}, \tag{3.2}$$

$$c_v\frac{\partial \tilde{T}}{\partial t} = -\overline{p'\frac{\partial u_j'}{\partial x_j}}, \tag{3.3}$$

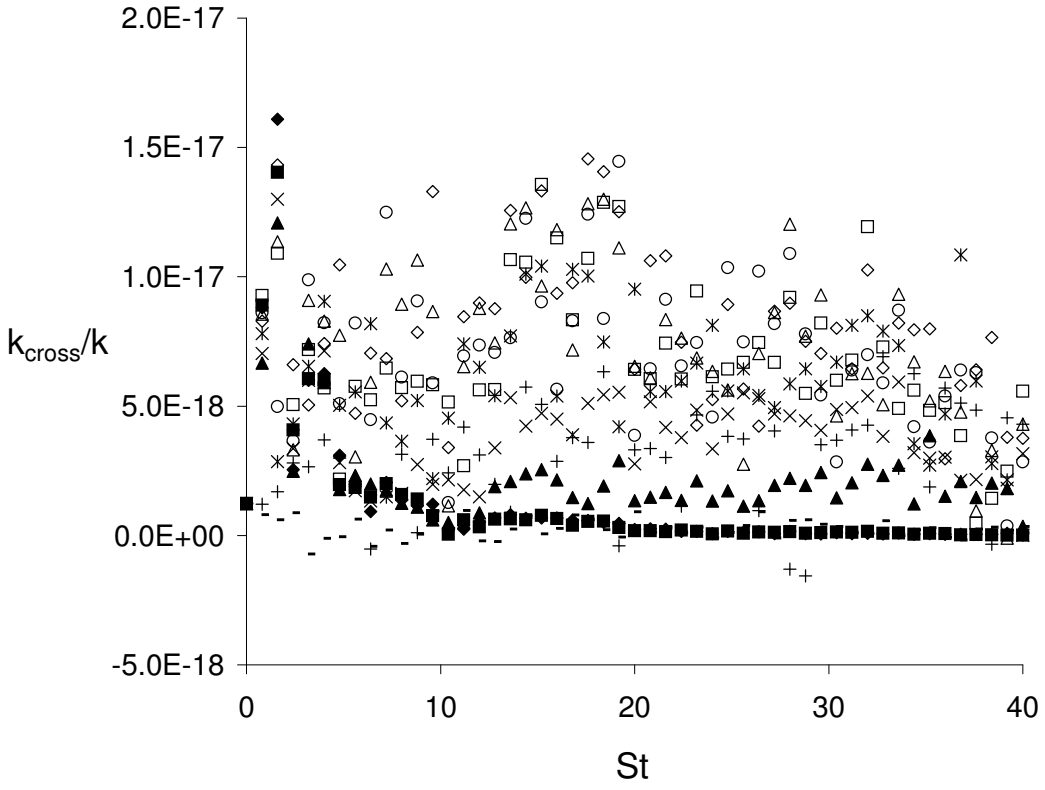

Fig. 9. Normalized kinetic energy component plots with solenoidal initial conditions for the cross component of kinetic energy. Plotted for a range of gradient Mach numbers M_g: $-$: 0.01; $+$: 0.29; $*$: 0.72; $\circ$:1.00; $\triangle$: 1.44; $\Diamond$: 2.88; $\square$: 5.76; $\times$: 14.4; $\blacktriangle$: 28.8; $\blacklozenge$: 288; $\blacksquare$: 2880.

respectively. Eq. (3.2) describes the evolution of the kinetic mode, while Eq. (3.3) describes the evolution of the internal mode through density-weighted mean temperature, $\tilde{T}$ (though temperature has been Reynolds-averaged, the Reynolds-averaged components can be represented using a density-weighted temperature). As can be seen, pressure-dilatation (i.e. the righthand side of both equations) is the link between the two equations. As kinetic energy is removed by pressure-dilatation, there is a corresponding increase in the thermal mode; conversely, a fall in internal energy due to pressure-dilatation will result in an increase in kinetic energy.

The next step is to track how much energy is being diverted away from kinetic energy and converted to internal energy. One way of doing this is to calculate the evolution of the mean temperature of the flow via integrating Eq. (3.3). This is a major benefit in deriving the equations as was described in Chapter II, in which the ideal gas law is employed rather than the isentropic gas relation, so that mean temperature can now be accounted for to see if contribution to the internal mode is significant (note that though, for the homogeneous shear case, temperature is the only mean parameter that grows with time, this is not necessarily so with other types of shear flows). Internal energy added to the system (as a fraction of total work inserted into the flow by production) and mean temperature growth are plotted in Figs. 10 and 11, respectively.

From Fig. 10, the incompressible condition ($M_g = 0.01$) remains practically zero for most of the simulation time (note that the trends become singular as $St \to 0$, since the plot is of the change in internal energy as a fraction of total work performed on the flow and total work is initially zero). While the internal energy change for $M_g = 0.01$ is practically zero (and, thus, mean temperature remains practically unchanged for the same case), internal energy grows significantly in a range of gradient Mach numbers from 0.72 to 5.76. Then, as $S \to \infty$, the internal energy fraction present in the flow

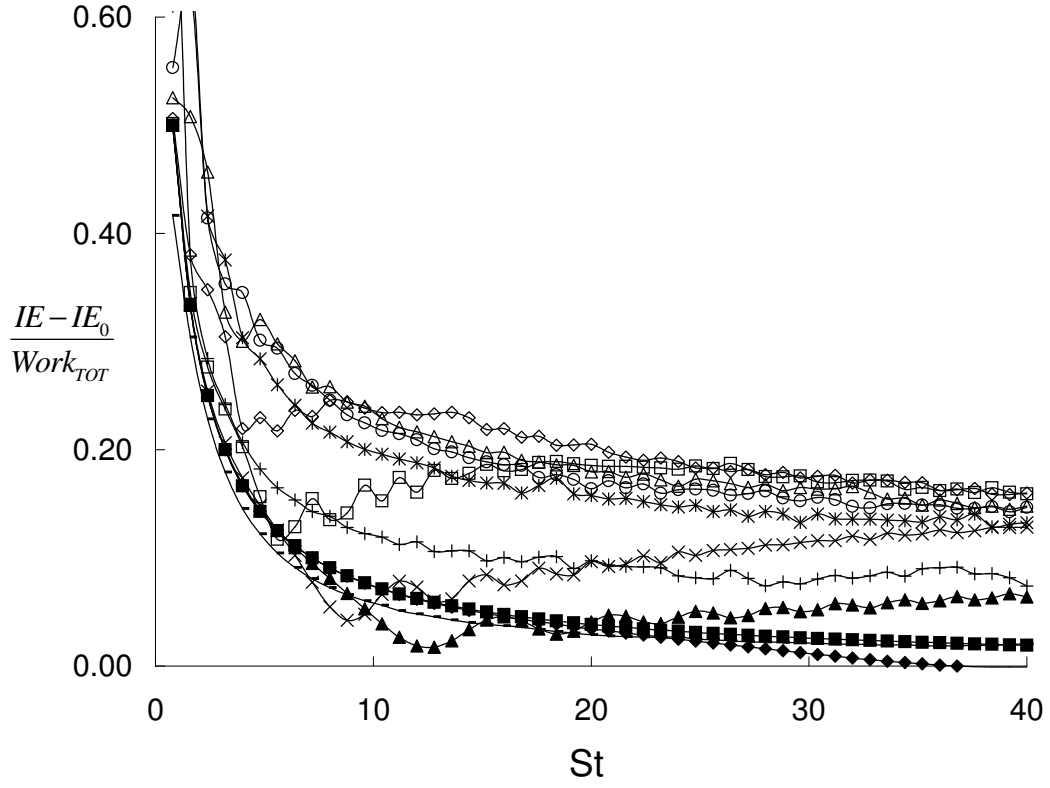

Fig. 10. Evolution of internal energy as a fraction of total work done by production, for initially-solenoidal turbulence. Plotted for a range of gradient Mach numbers M_g: −: 0.01; +: 0.29; ∗: 0.72; ∘:1.00; △: 1.44; ♢: 2.88; □: 5.76; ×: 14.4; ▲: 28.8; ♦: 288; ■: 2880.

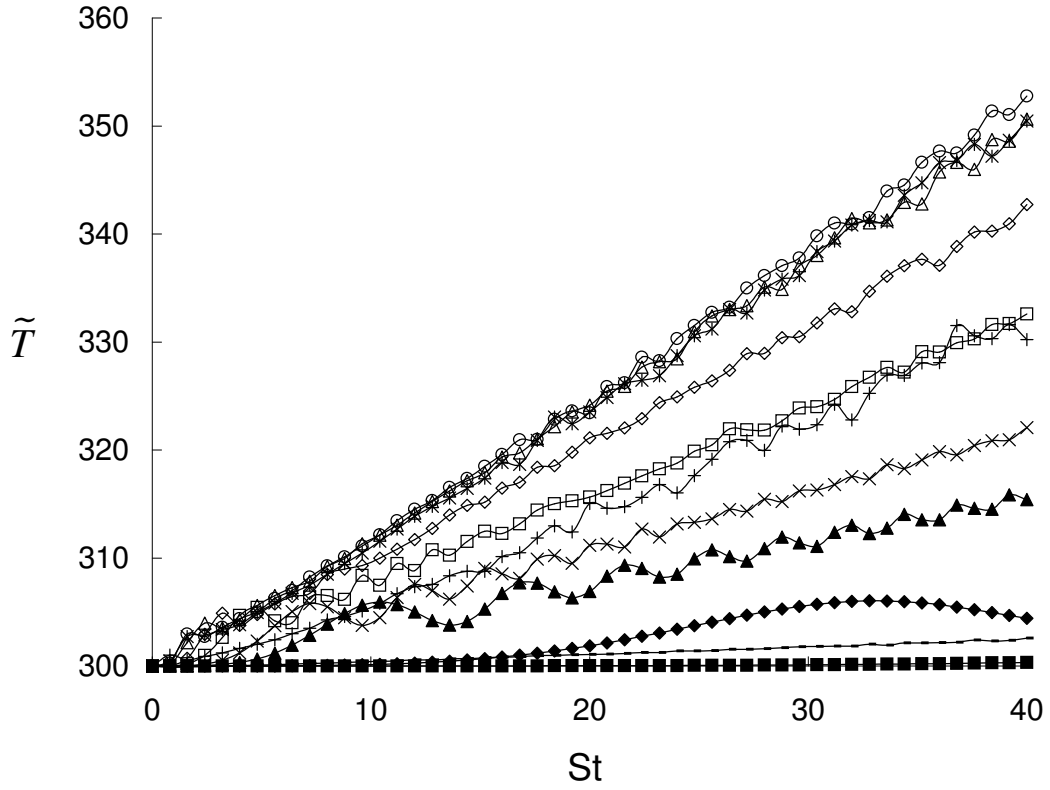

Fig. 11. Evolution of density-weighted mean temperature for initially-solenoidal initial conditions. Plotted for a range of gradient Mach numbers M_g: $-$: 0.01; $+$: 0.29; $*$: 0.72; $\circ$:1.00; $\triangle$: 1.44; $\Diamond$: 2.88; $\square$: 5.76; $\times$: 14.4; $\blacktriangle$: 28.8; $\blacklozenge$: 288; $\blacksquare$: 2880.

is driven back to zero (which is also reflected in Fig. 11, as mean temperature also remains unchanged for large values of M_g). This is intuitive since the ever-increasing inertia of the flow gives dominance to the production, requiring a larger relative timescale for pressure to act on the flow (which isn't to say that the internal energy won't grow with time for the high-shear case; certainly, as pressure is given more time to act, some kinetic energy will eventually be converted to internal energy). Therefore, as we state that pressure-dilatation is responsible for this conversion of energy from the kinetic mode to the internal mode, this has been somewhat shown to be true by the results as there is no dilatation at the incompressible limit and there is no pressure at the Burgers limit. The conclusion is that the amount of internal energy relative to work being done by the mean shear is large for 0.72 to 5.76 in the time observed; however, this is not necessarily indicative of the gradient Mach number at which the maximum amount of internal energy is produced; to obtain this information, we must observe the growth of the mean temperature.

The maximum mean temperature growth occurs at approximately $M_g = 1.00$, an interim gradient Mach number. Indeed, at $M_g = 1.00$, the necessity to include the energy equation becomes apparent as mean temperature grows by over 17% of the initial value. It was shown earlier that the maximum conversion of kinetic energy from the solenoidal mode to the dilatational mode occurs for this gradient Mach number. Therefore, it can be seen that the unique behavior that has so far been observed is a result of the pressure-dilatation (i.e. $\langle pd \rangle$, the coupling of the momentum and internal energy equations) becoming most active at approximately $M_g = 1.00$ (see Fig. 12, where data is plotted to $St = 5$; maximum amplitude of $\langle pd \rangle$ occurs for $M_g = 1.00$ at about $St = 1.5$). Similarly, previous research [5] also finds maximum pressure-dilatation occurring at an interim Mach value near the incompressible limit.

Since pressure-dilatation is a maximum for approximately $M_g = 1.00$, it appears

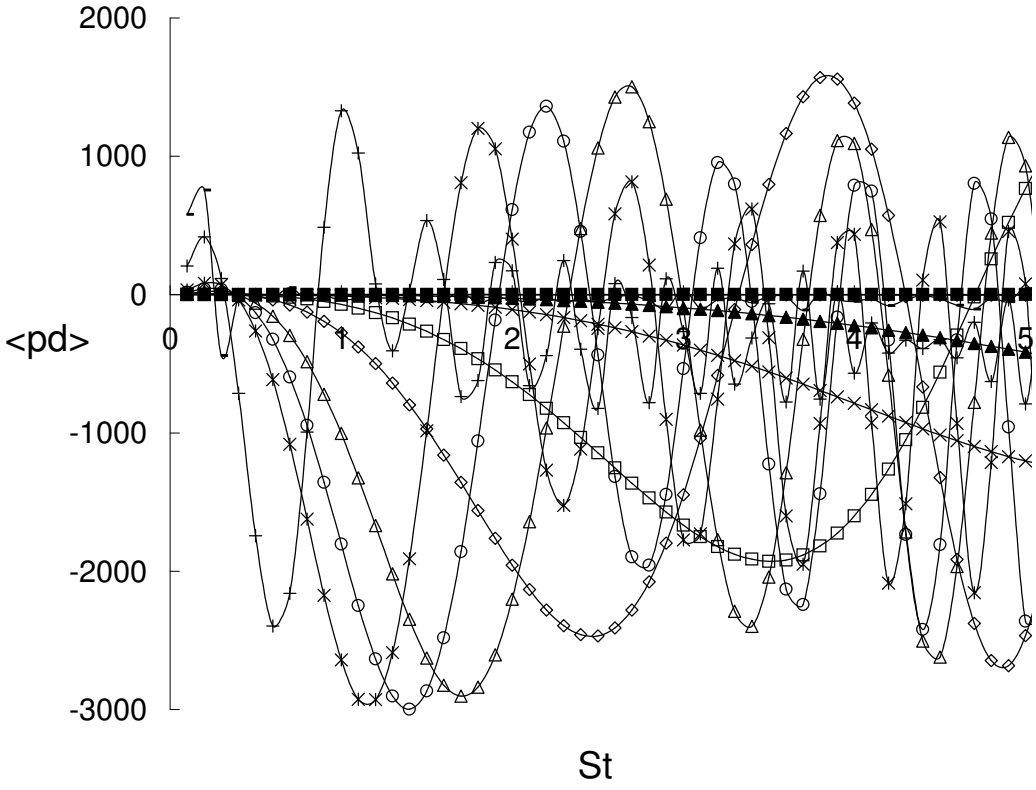

Fig. 12. Evolution of pressure-dilatation for initially-solenoidal turbulence. Plotted for a range of gradient Mach numbers M_g: $-$: 0.01; $+$: 0.29; $*$: 0.72; $\circ$:1.00; $\triangle$: 1.44; $\Diamond$: 2.88; $\square$: 5.76; $\times$: 14.4; $\blacktriangle$: 28.8; $\blacklozenge$: 288; $\blacksquare$: 2880.

plausible that the size of $\langle pd \rangle$ determines not only the ease of transfer of kinetic energy from the solenoidal to dilatational mode, but also the ease of transfer of energy from the kinetic to the internal mode. Pressure-dilatation can be viewed as a valve between the two modes; the size of $\langle pd \rangle$ determines the ease of transfer of energy between the two modes.

It seems a bit more than coincidental that maximum temperature growth occurs at $M_g = 1.00$. A possible conclusion that can be drawn from this is that, when the shear and acoustic timescales are equal, an optimal coupling of the momentum and energy occurs. To validate this conclusion, several simulations are performed with various initial temperatures, with shear adjusted according to Eq. (2.24), and their results are plotted in Fig. 13. It can be clearly seen that, no matter the initial conditions for temperature, the maximum coupling between momentum and energy takes place at $M_g = 1.00$ for an initially-incompressible flow.

Fig. 10 also shows that, as $St \rightarrow \infty$, the internal energy fraction eventually reaches some Mach-independent constant value. So, though energy is continually being added via the constantly-applied shear, a balance is eventually reached in the division between the kinetic and internal modes (though it seems to take longer for this balance to be reached as M_g is increased). That is, the ratio of energy supplied to kinetic-to-internal modes reaches a constant at large St.

C. Three Distinct Regions of R-RDT

The observations that have been made thus far allow some generalizations to be made about R-RDT. By isolating just the $M_g = 14.4$ case and comparing it with the incompressible and Burgers limits, we can observe three distinct regions present with R-RDT: an initially shear-dominant region, a region characterized by increasing

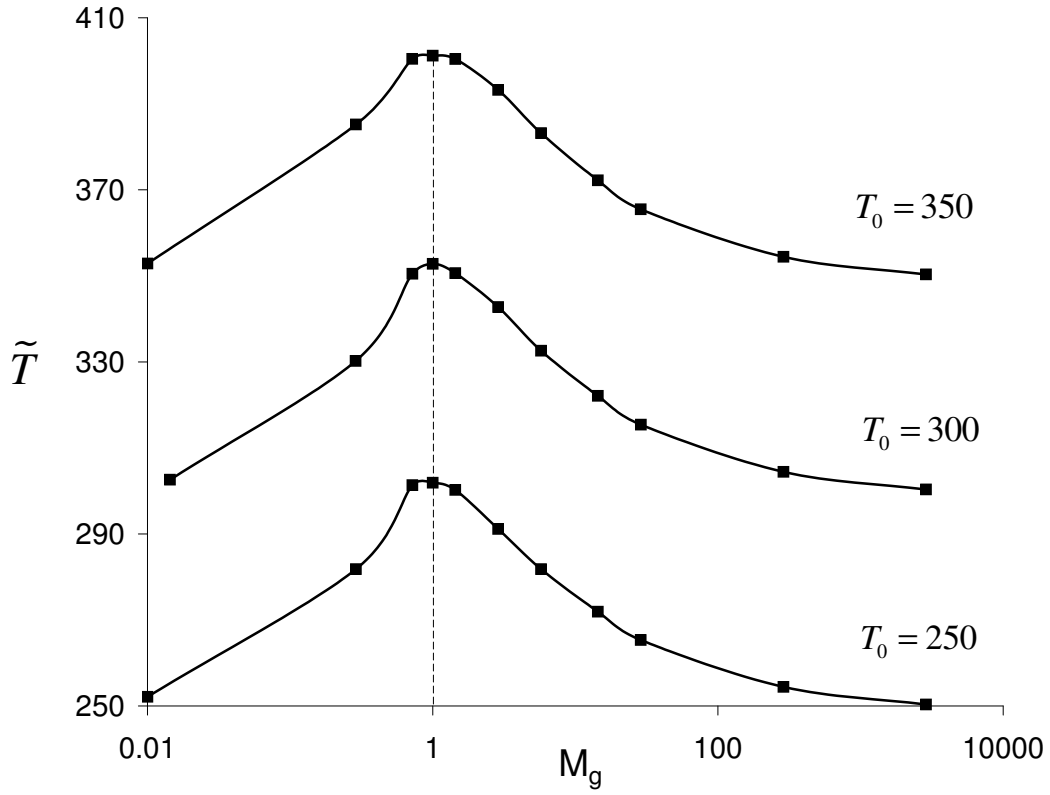

Fig. 13. Density-weighted temperature at $St = 40$ for various values of initial temperature, as specified.

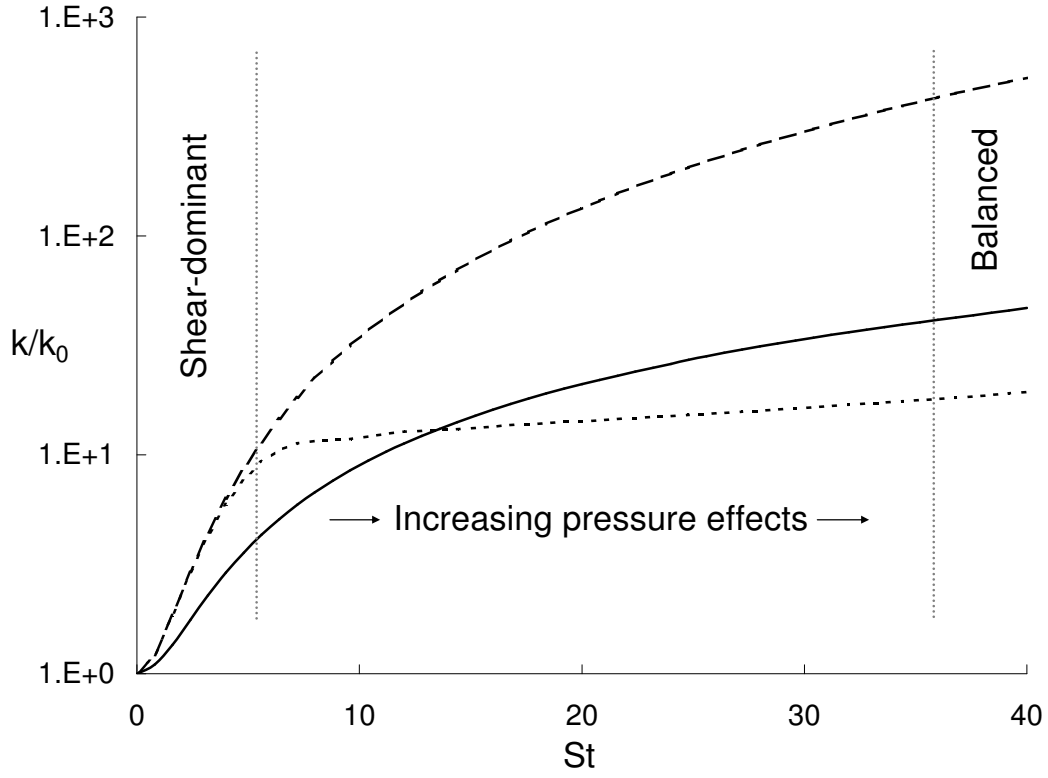

Fig. 14. Kinetic energy evolution showing three distinct regions present in R-RDT equations. Solid line: incompressible limit; dashed line: Burgers limit; dotted line: $M_g = 14.4$.

pressure effects and a balanced region where the shear-to-pressure ratio reaches a self-similar state (see Fig. 14).

At early times, the shear-dominant region forces the kinetic energy evolution to follow the Burgers (no-pressure) case, which should come as no surprise since the high shear essentially nullifies the effects of pressure in the calculation. However, as was noted earlier, the effects of pressure increase with time due to the growth of $\widehat{\kappa}_2$. This is evident as all the terms in Eq. (2.21a) that stem from the pressure gradient in the governing momentum equation are multiplied by $\widehat{\kappa}_2$. Additionally, though the wavevectors are initially evenly distributed, they tend in time toward the

$\widehat{\kappa}_2$ component, as seen in Fig. 15 and as is the case in incompressible RDT [2]. As pressure begins to influence the flow, oscillatory effects creep into the kinetic energy evolution and peel it away from the Burgers solution. It is in this second region where pressure begins to neutralize the shear dominance. It is also in this region where little to no production is taking place as b_{12} (the anisotropy component directly linked to production) is approximately zero in this region (as can be seen in Fig. 16). Finally, a third region is reached where the oscillations are damped out, b_{12} decreases from zero toward the non-zero incompressible solution and a balance is reached between shear and pressure similar to that in incompressible flow.

When examining the behavior of the b_{12} anisotropy component, comparison can be made to previous RDT [13] and direct numerical simulation (DNS) [18] homogeneous shear turbulence. In this previous work, the isentropic gas equation is used to calculate pressure and, thus, the energy equation is not incorporated; as a result, thermodynamic effects are not addressed. Previous RDT results [13] are found to generally match the trends of the DNS results for b_{12} and Λ (i.e. the turbulent kinetic energy growth rate exponent), with similar magnitudes for each (see Figs. 17 and 18, respectively). Both sets of results also document the behavior in kinetic energy evolution mentioned earlier - i.e. that kinetic energy increases monotonically with increasing Mach number at early St, while kinetic energy switches to decrease monotonically with increasing Mach number at long St, with the "crossover" point occurring at $St \approx 4$. The DNS of the b_{12} component is found to be sensitive to the Mach number as it reaches an asymptotic state at long St; however, the RDT data of Simone *et al.* shows that b_{12} tends to converge to a single value, irrespective of the gradient Mach number. The reasoning given [13] is that disregarding the non-linear terms in RDT aids in capturing the general trends and magnitudes, but neglects important effects that characterize the flow at long St. Similar trends and magnitudes

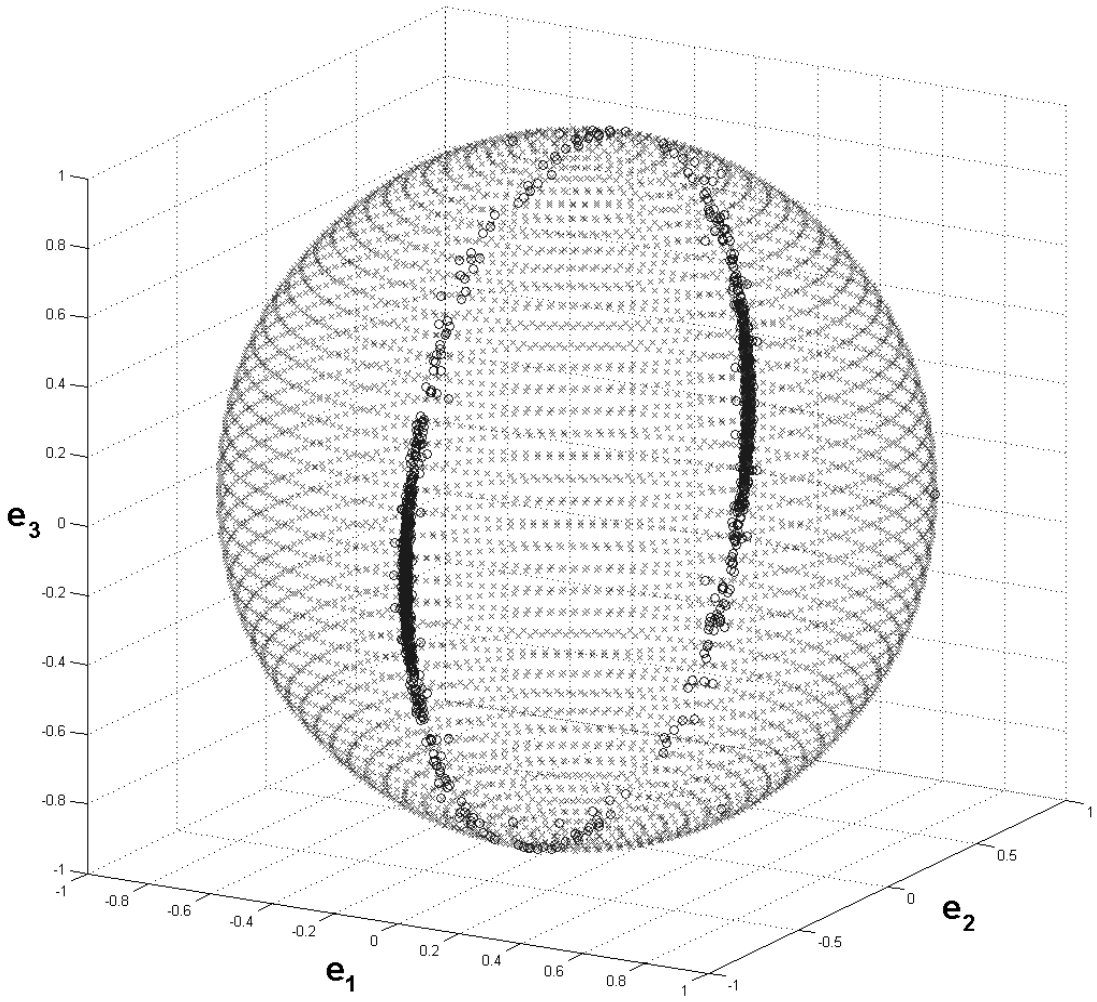

Fig. 15. Evolution of unit wavevectors with time for the $M_g = 1.00$ case, showing the progression toward the e_2 unit direction. Symbols represent: $\times$: initial position of wavevectors; $\circ$: position of wavevectors at $St = 40$

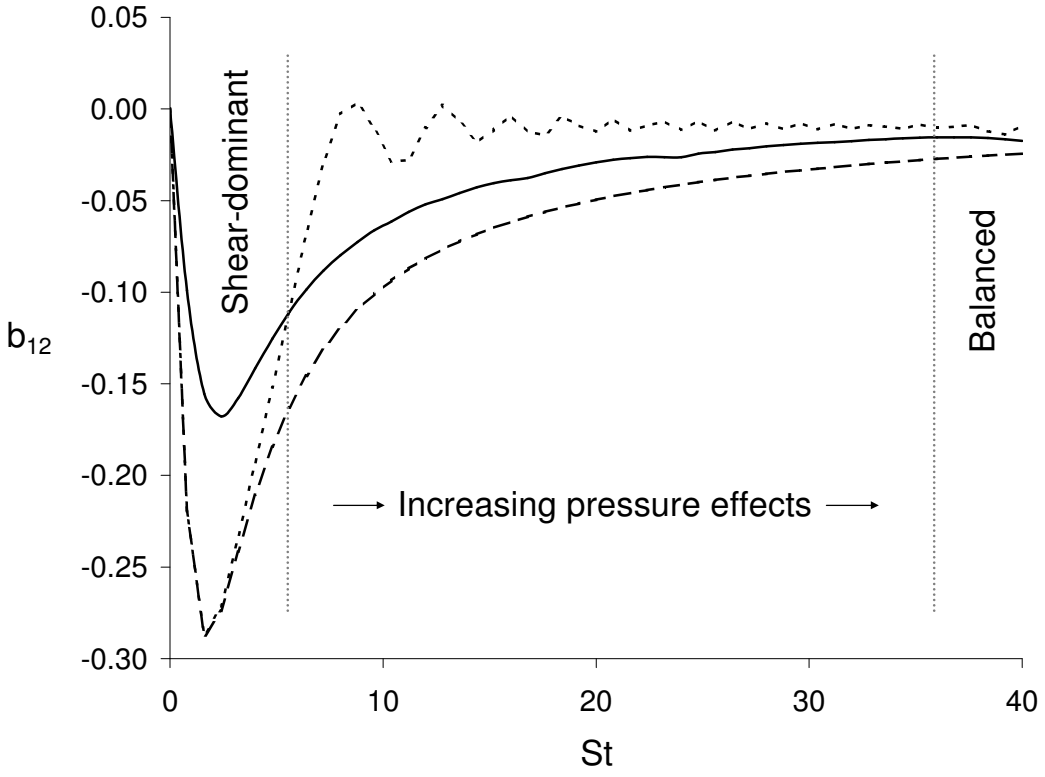

Fig. 16. b_{12} anisotropy evolution showing three distinct regions present in R-RDT equations. Solid line: incompressible limit; dashed line: Burgers limit; dotted line: $M_g = 14.4$.

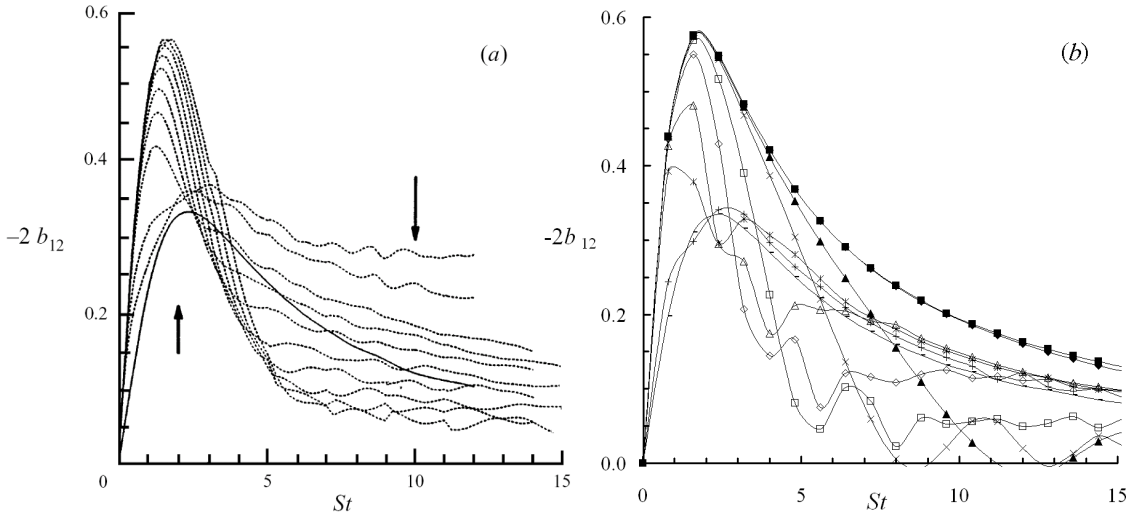

Fig. 17. b_{12} anisotropy component of initially-incompressible homogeneous turbulence in pure shear at various Mach numbers. Plots are shown for (a) DNS [18] (with the solid line indicating incompressible limit and arrows the direction of increasing Mach number) and (b) R-RDT (symbols indicating values of M_g: $-$: 0.01; $+$: 0.29; $*$: 0.72; $\circ$:1.00; $\triangle$: 1.44; $\Diamond$: 2.88; $\square$: 5.76; $\times$: 14.4; $\blacktriangle$: 28.8; $\blacklozenge$: 288; $\blacksquare$: 2880.)

of b_{12} and Λ are found with R-RDT, including the crossover point occurring at $St \approx 4$ and the b_{12} anisotropy component converging to a common value at long St.

The b_{12} component in the previous research [13] is also divided into solenoidal and dilatational components so that the role of compressibility can be examined (via increasing Mach number) on each portion of the flow and then compared with the DNS data. In R-RDT as well, both the trends and magnitudes match very well with the DNS data for b_{12} for both the solenoidal and dilatational fields, as shown in Figs. 19 and 20, respectively.

One analogy for interaction between shear and pressure and how they affect kinetic energy is that of a mass (which is attached to a vertical spring that is fixed at one end) suddenly dropped from rest (see Fig. 21). Initially in Fig. 21a, the mass

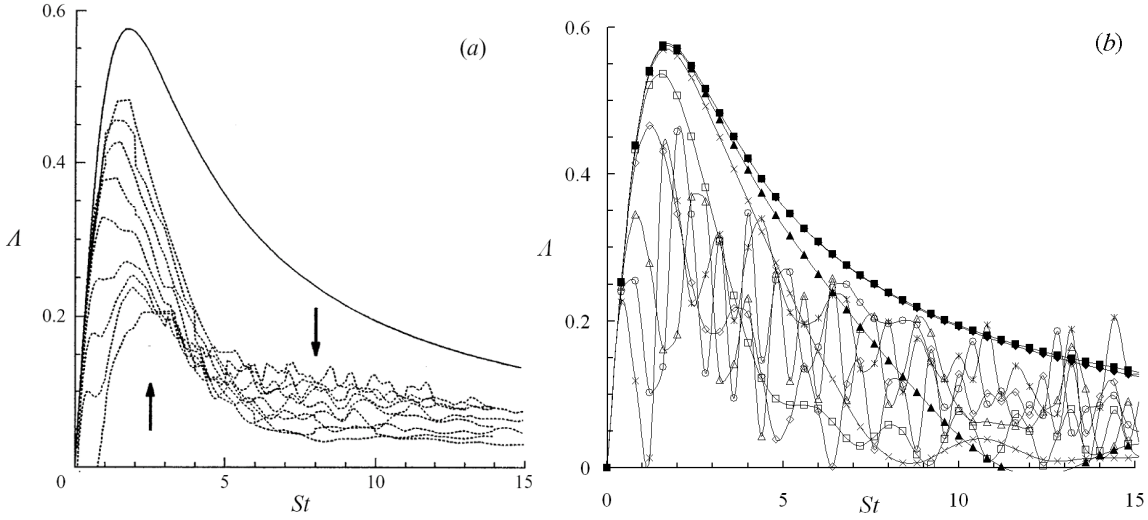

Fig. 18. Turbulent kinetic energy growth rate exponent of initially-incompressible homogeneous turbulence in pure shear at various Mach numbers. Plots are shown for (a) DNS [18] (with the solid line indicating Burgers limit and arrows the direction of increasing Mach number) and (b) R-RDT (symbols indicating values of M_g: $*$: 0.72; $\circ$:1.00; $\triangle$: 1.44; $\Diamond$: 2.88; $\square$: 5.76; $\times$: 14.4; $\blacktriangle$: 28.8; $\blacklozenge$: 288; $\blacksquare$: 2880.

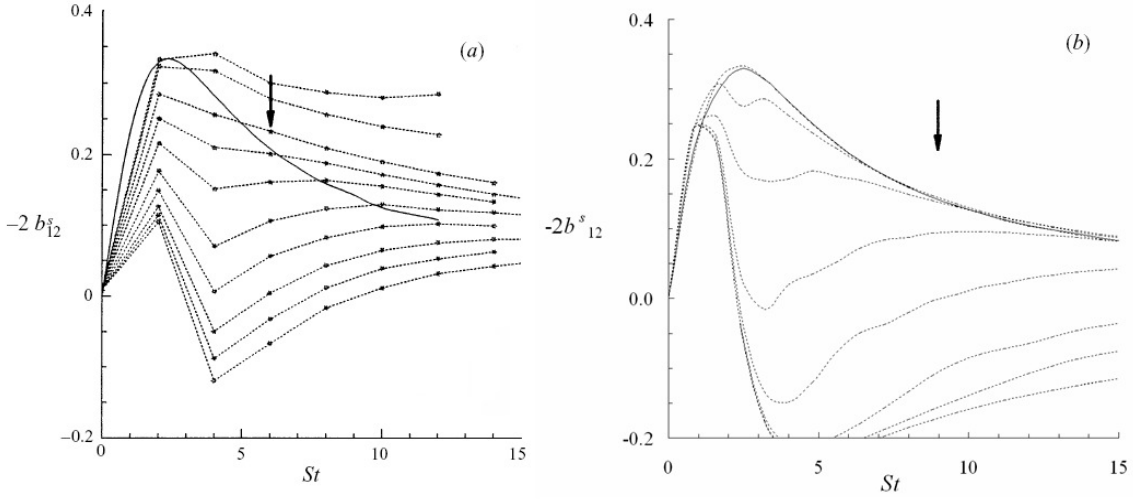

Fig. 19. Solenoidal b_{12} anisotropy component of initially-incompressible homogeneous turbulence in pure shear at various Mach numbers (arrows indicate direction of increasing Mach number). Solid line represents the incompressible limit. Plots are shown for (a) DNS [18] and (b) R-RDT.

is released. The downward force on the mass caused by gravity (similar to shear) is opposite and greater than the force applied by the spring (similar to pressure, especially so since pressure is known to provide elasticity to the flow), causing the mass to accelerate downward. The inertia of the mass stretches the spring to its maximum length until finally the force of the spring is large enough to counteract the weight of the object and accelerate it upward; the mass moves upward and slows until the force of gravity can again override the force from the spring; this process produces ever-dampening oscillations (Fig 21b). These oscillations continue until the gravitational force balances the force from the spring, causing the mass to come to rest at a point between its starting position and its greatest extension (Fig. 21c).

This analogy is not a perfect one, as the energy via the production term (b_{12}) does not oscillate exactly about the incompressible limit. It seems that the increase

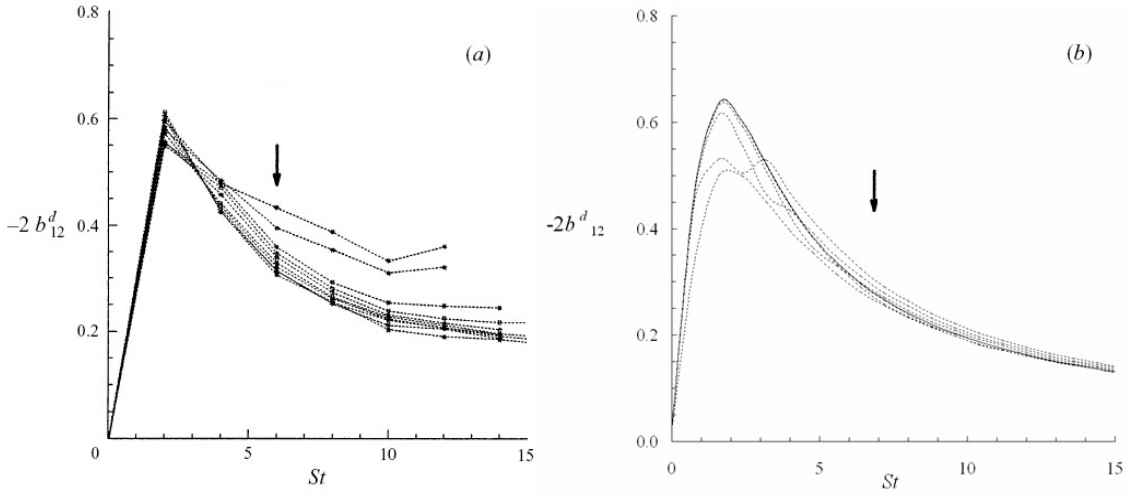

Fig. 20. Dilatational b_{12} anisotropy component of initially-incompressible homogeneous turbulence in pure shear at various Mach numbers (arrows indicate direction of increasing Mach number). Solid line represents the Burgers limit. Plots are shown for (a) DNS [18] and (b) R-RDT.

of dilatational kinetic energy in the "oscillation" region correlates very well to the amount of departure of production from the incompressible limit (see Fig. 8). It is possible that the dilatational portion of the flow actually serves to provide additional elasticity to the flow (similar to an additional spring) and saps some of the energy growth that would have otherwise been experienced by the system. However, the spring analogy is useful in gaining a better understanding of the physical processes at work in the rapidly-distorted limit.

With the above discussion about the three distinct regions in R-RDT, it should also be noted that kinetic energy in Fig 14 is plotted versus shear-time, so that the relative sizes of the first two regions are stretched in size with higher values of M_g. In a more physically realistic timescale (e.g. acoustic time), the first two regions occur very rapidly. In fact, the Burgers limit is an infinitely-stretched shear-dominant

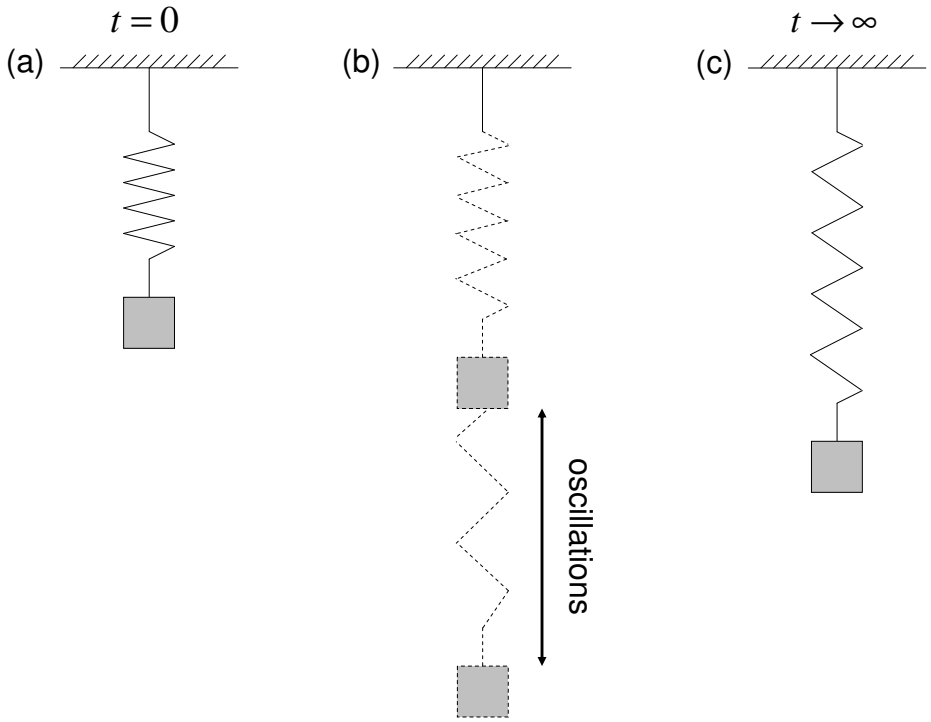

Fig. 21. Analogy of a spring-mass system with mass dropped from rest, describing three regions of R-RDT: (a) initially, at the point the mass is released; (b) after release of the mass during oscillations up and down; (c) at long time when the mass comes to rest.

region (i.e. as $M_g \to \infty$), while the incompressible limit has an infinitely-stretched self-similar region (i.e. as $M_g \to 0$). The relative sizes of all three regions varies as M_g is varied. In practice, the shear-dominant region may not be of much physical relevance; however, for understanding the behavior in the rapid distortion limit, it is important to note the distinction.

D. Effect of Initial Dilatation

To view the role of pressure-dilatation from another perspective, we vary the initial conditions so that the flow is now initially fully dilatational (by aligning the velocity fluctuations along the $\widehat{\kappa}_3$ wavevector component). Initial conditions are scaled such that total initial energy remains constant across the two cases and the Reynolds stress tensor is kept isotropic so that the effects of dilatation can be isolated. A plot of the turbulent kinetic energy present in the flow for initially-dilatational turbulence can be found in Fig. 22.

The trends for the kinetic energy evolution for the initially-dilatational case look similar to the initially-solenoidal case (Fig. 5), with the plots peeling off from the Burgers solution toward the incompressible solution. The trend of the curves at the low-Mach limit for the initially-compressible case do not match the solenoidal incompressible RDT results, as expected. In fact, for low Mach numbers where pressure is more dominant over shear, the compressibility of the initial conditions allows for reverse flow of energy from the kinetic mode to the internal mode (as shown by the initial dip below initial kinetic energy for $M_g \leq 1.44$ in Fig. 5). And though the Burgers solution remains the same for both cases, the kinetic energy levels of the initially-dilatational case are generally less than those for the initially-solenoidal case at lower value of M_g. The fact that the Burgers solution (in which pressure-dilatation

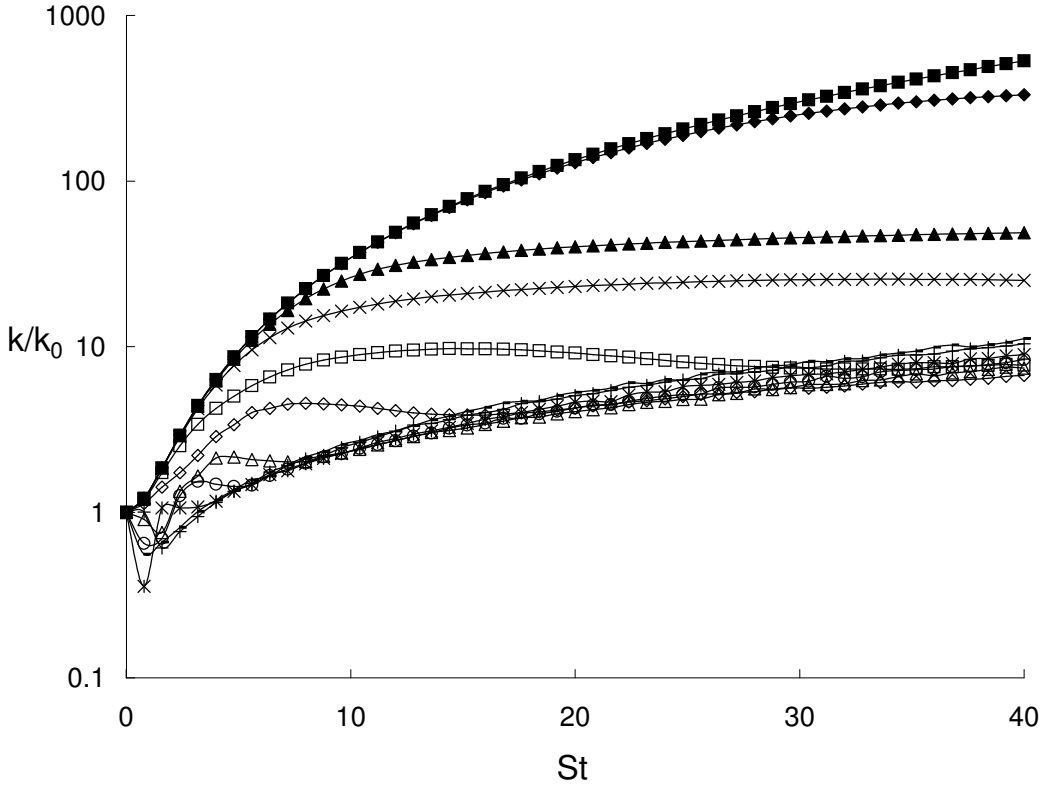

Fig. 22. The evolution of normalized turbulent kinetic energy with dilatational initial conditions. Plotted for a range of gradient Mach numbers M_g: $-$: 0.01; $+$: 0.29; $*$: 0.72; $\circ$:1.00; $\triangle$: 1.44; $\Diamond$: 2.88; $\square$: 5.76; $\times$: 14.4; $\blacktriangle$: 28.8; $\blacklozenge$: 288; $\blacksquare$: 2880.

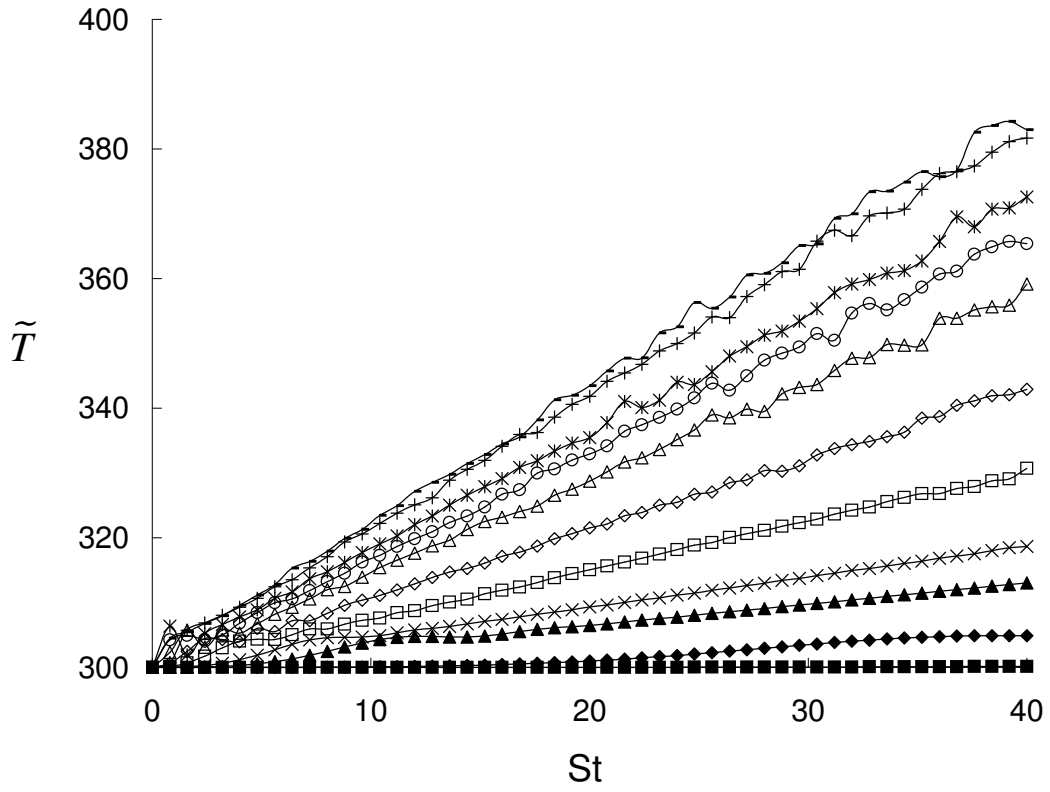

Fig. 23. Evolution of density-weighted mean temperature for initially-dilatational initial conditions. Plotted for a range of gradient Mach numbers M_g: $-$: 0.01; $+$: 0.29; $*$: 0.72; $\circ$:1.00; $\triangle$: 1.44; $\Diamond$: 2.88; $\square$: 5.76; $\times$: 14.4; $\blacktriangle$: 28.8; $\blacklozenge$: 288; $\blacksquare$: 2880.

has no part) remains constant indicates, at least at that limit, that the same amount of energy is being inserted into the flow; so the fact that the plots of kinetic energy of the smaller values of M_g are themselves smaller (mainly for $M_g \leq 5.76$) may be an indication that more energy is being transferred to the thermal mode. To examine this possibility, the mean temperature and internal energy as a fraction of total work done on the flow for the initially-dilatational case are plotted in Figs. 23 and 24, respectively.

The mean temperature plot in Fig. 23 shows that total temperature of the

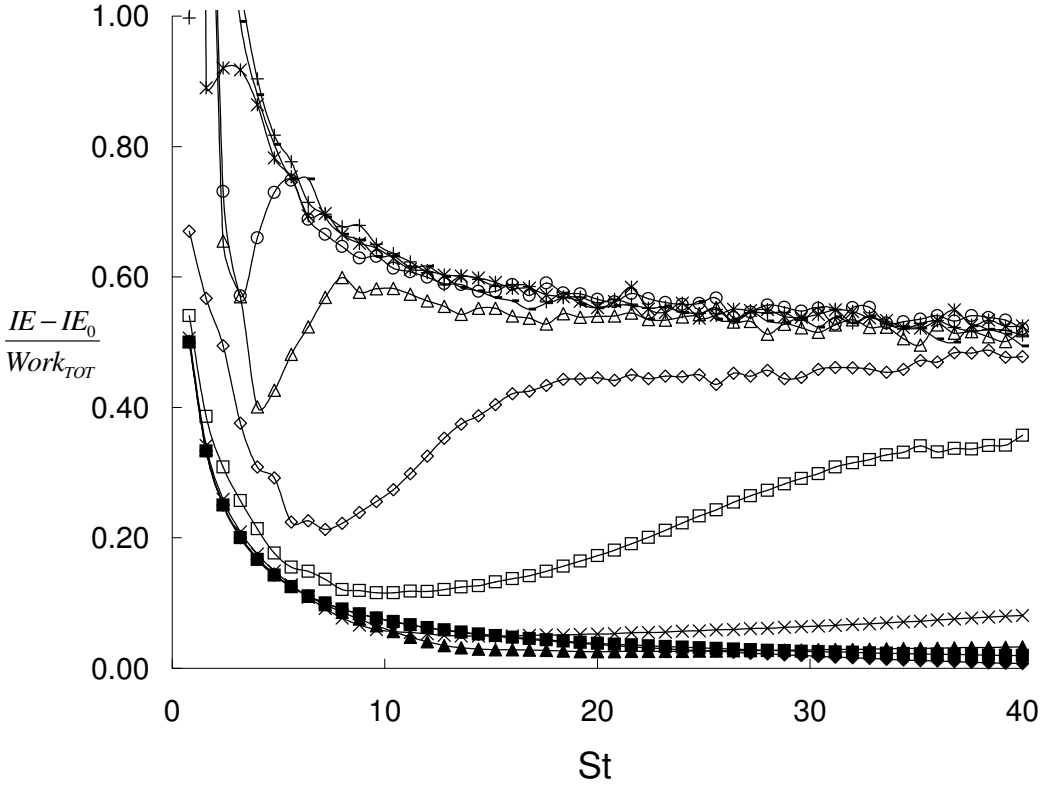

Fig. 24. Evolution of internal energy as a fraction of total work done by production, for initially-dilatational turbulence. Plotted for a range of gradient Mach numbers M_g: −: 0.01; +: 0.29; ∗: 0.72; ○:1.00; △: 1.44; ◇: 2.88; □: 5.76; ×: 14.4; ▲: 28.8; ♦: 288; ■: 2880.

flow increases for most cases as compared to the initially-solenoidal case (Fig. 11), the most significantly for $M_g \leq 5.76$, whereas the higher shear cases do not change significantly. So it seems that $\langle pd \rangle$ in the initially-dilatational case is more effective in converting energy to the thermal mode for $M_g \leq 5.76$ (i.e. as the incompressible limit is approached). This can also be observed in Fig. 24, where the internal energy fraction is higher for $M_g \leq 5.76$ (at about 60%) than for the solenoidal case in Fig. 10. Also evident from Fig. 23 is that the gradient Mach number of maximum mean temperature growth shifts downward from about $M_g = 1.00$ in the initially-solenoidal case to the incompressible limit, $M_g = 0.01$, for the initially-dilatational case.

As was performed for the initially-solenoidal case, the kinetic energy is again partitioned into solenoidal and dilatational components and plotted in Figs. 25 and 26, respectively. From the component plots of kinetic energy, it can be seen that all of the energy initially lies in the dilatational field, as expected from our initial conditions. Additionally, for the incompressible case ($M_g = 0.01$), the entirety of the energy remains in the dilatational field; when dilatational energy is a maximum, it seems that mean temperature growth is also a maximum. However, the figures show that increasing the mean shear drives the energy to the solenoidal field at early times.

These trends of the solenoidal and dilatational components of kinetic energy for the initially-dilatational case are different from those for the initially-solenoidal case (Fig. 8) in that more kinetic energy is retained in the dilatational field for low values of shear ($M_g \leq 5.76$), as increasing shear seems to force the flow back to the solenoidal mode. This is a consistent theme with the initially-dilatational case, that compressibility in the initial conditions has the greatest effect on the lower-shear cases, which leads to greater efficiency of pressure-dilatation converting energy to the internal mode.

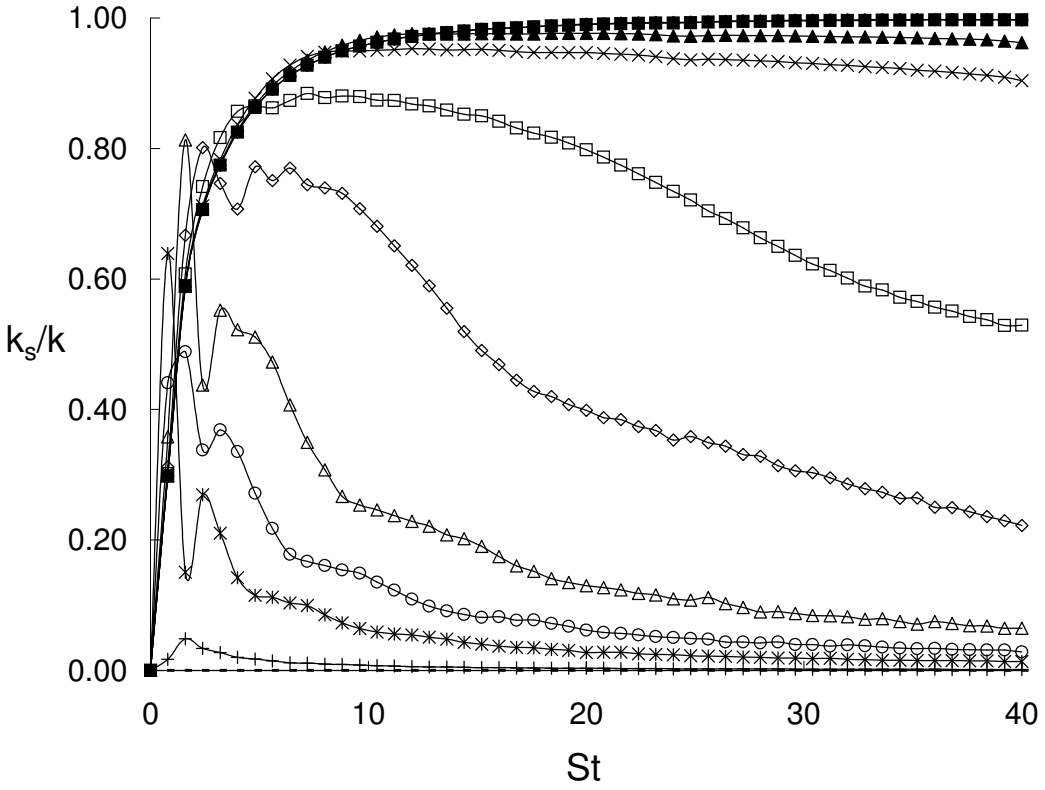

Fig. 25. Normalized solenoidal kinetic energy plots with dilatational initial conditions. Plotted for a range of gradient Mach numbers M_g: −: 0.01; +: 0.29; ∗: 0.72; ∘:1.00; △: 1.44; ♢: 2.88; □: 5.76; ×: 14.4; ▲: 28.8; ♦: 288; ■: 2880.

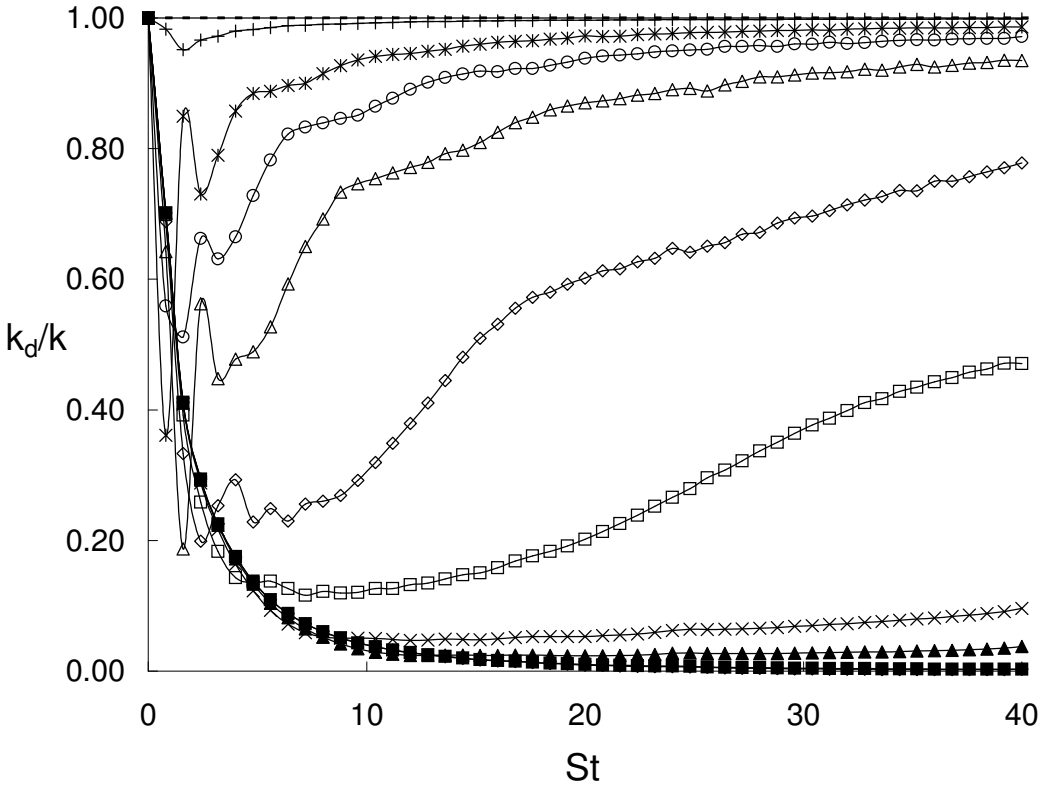

Fig. 26. Normalized dilatational kinetic energy plots with dilatational initial conditions. Plotted for a range of gradient Mach numbers M_g: −: 0.01; +: 0.29; ∗: 0.72; ○:1.00; △: 1.44; ◇: 2.88; □: 5.76; ×: 14.4; ▲: 28.8; ♦: 288; ■: 2880.

1. Superposability of R-RDT Equations

Varying the compressibility of the initial conditions allows the opportunity to test another facet of RDT, that being the linearity of the governing equations. As such, the R-RDT results should be superposable for various combinations of compressibility and incompressibility in the initial conditions.

To test the superposability of the R-RDT results, data is taken from the $M_g = 1.00$ case where the initial field is composed of 70% solenoidal energy and 30% dilatational energy. Then the two data sets obtained from the fully solenoidal and fully dilatational initially-conditioned cases for $M_g = 1.00$ are weighted by 70% and 30%, respectively, and are summed together. The comparison of what results is presented for two representative parameters - kinetic energy evolution and mean temperature evolution - in Figs. 27 and 28, respectively. A similar method is applied for the $M_g = 1.00$ case where the solenoidal and dilatational composition of the initial field is 30% and 70%, respectively, and is also plotted in Figs. 27 and 28.

It can be seen that this method of adding scaled components of the fully solenoidal and dilatational cases results in good agreement with the cases of mixed initial conditions. This confirms that the R-RDT equations are indeed linear and superposable, and that the results scale linearly from the initially-solenoidal data to the initially-dilatational data. This has important closure model implications.

2. Compressibility Effects on Anisotropy

Knowing that $\langle pd \rangle$ increases in efficiency (i.e. in effectiveness at converting work done on the system to internal energy) as the compressibility of the initial conditions is increased, we now seek to observe the effect of $\langle pd \rangle$ on the anisotropies as the compressibility of the initial conditions is increased. It is generally known that pressure

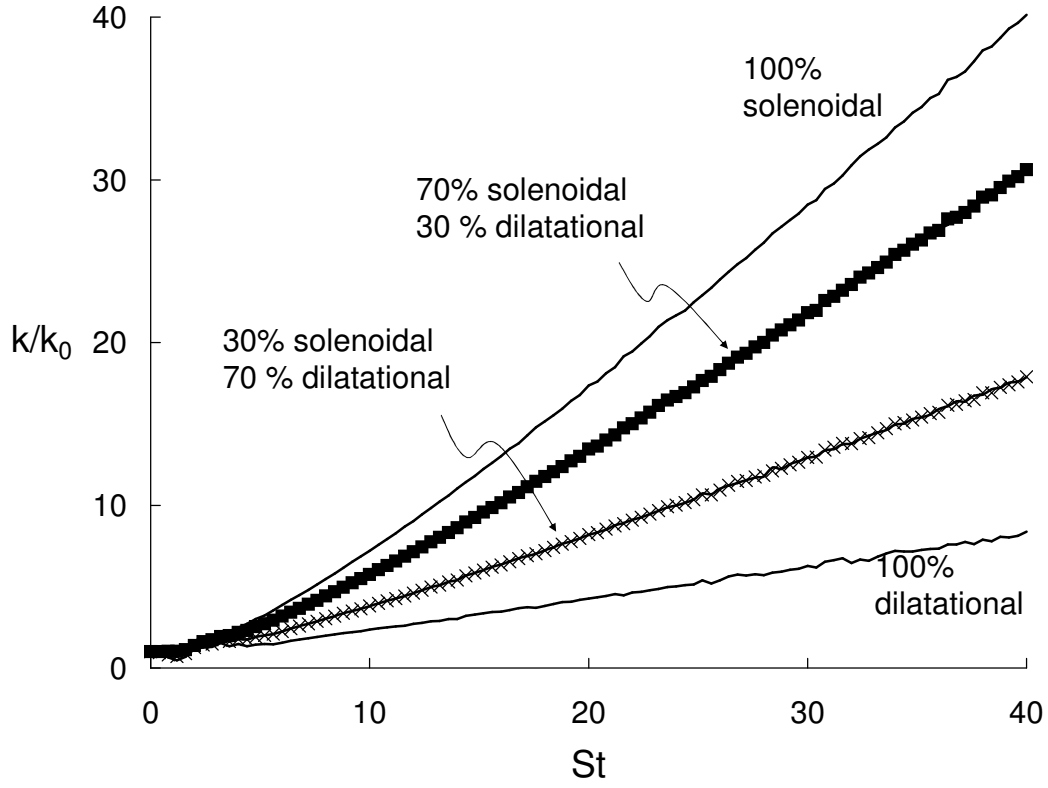

Fig. 27. Kinetic energy growth at various initial mixtures of compressibility and incompressibility for $M_g = 1.00$. Solid lines: results for specified initial mixtures; ■: results weighted 70% solenoidal and 30% dilatational; ×: results weighted 30% solenoidal and 70% dilatational.

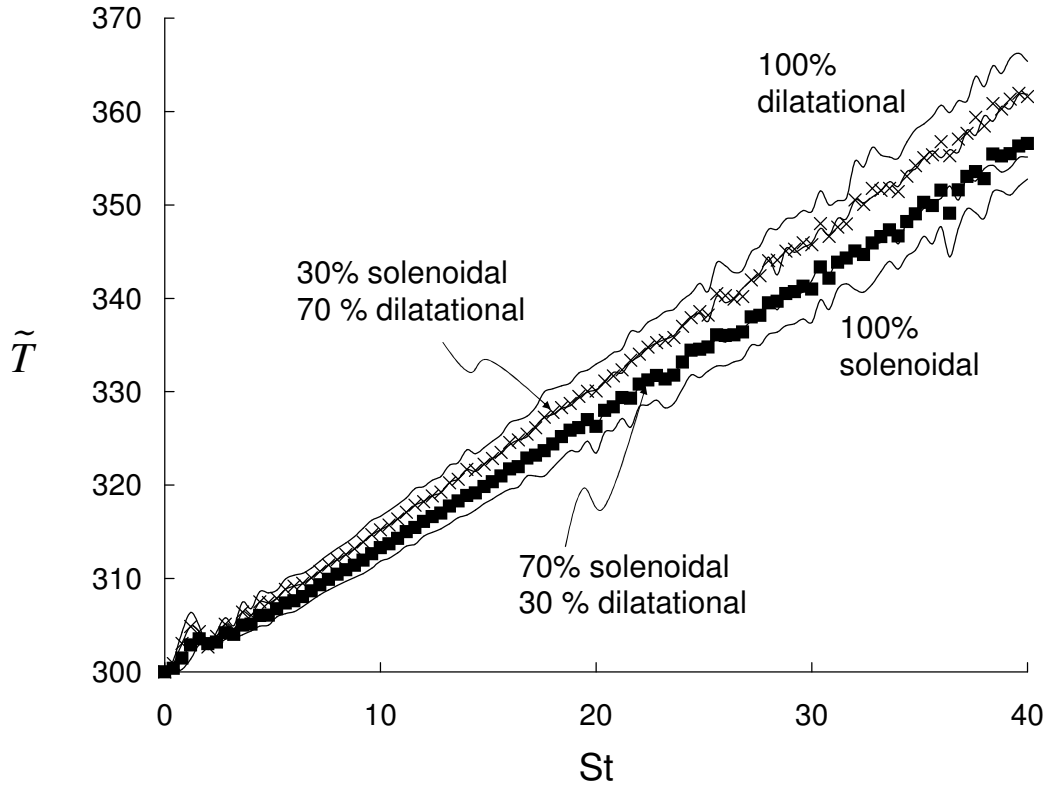

Fig. 28. Mean temperature growth at various initial mixtures of compressibility and incompressibility for $M_g = 1.00$. Solid lines: results for specified initial mixtures; ■: results weighted 70% solenoidal and 30% dilatational; ×: results weighted 30% solenoidal and 70% dilatational.

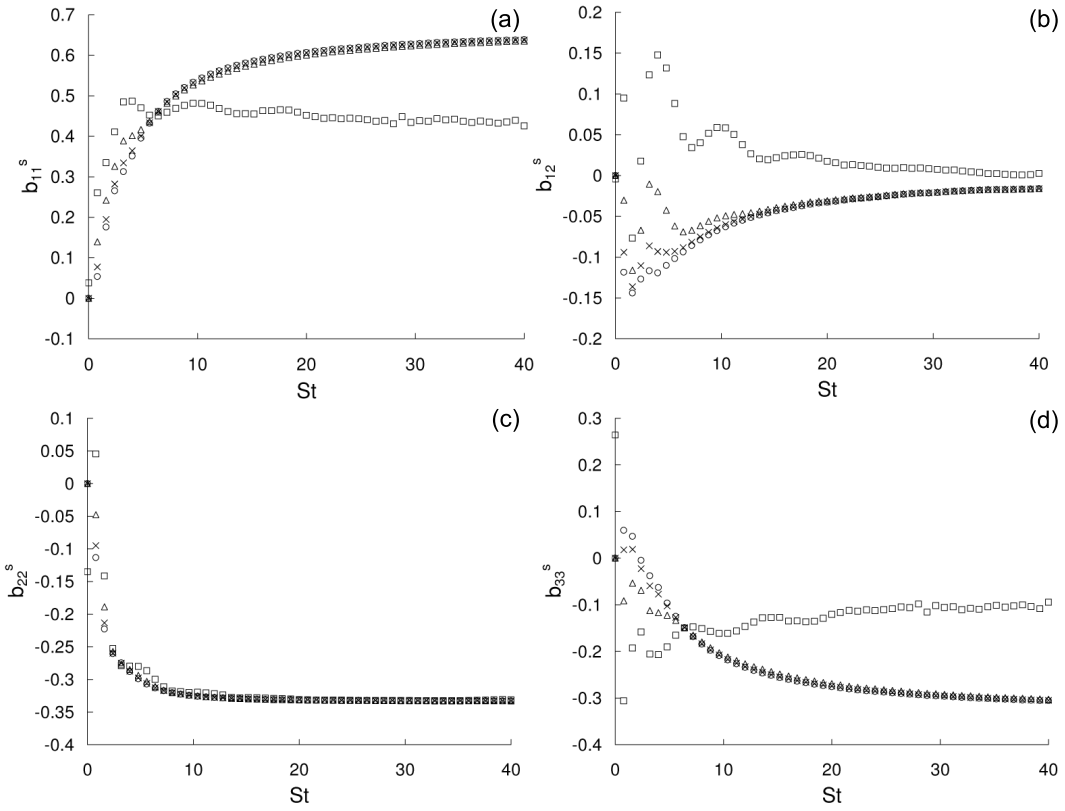

Fig. 29. Solenoidal, non-zero components of the anisotropy tensor for $M_g = 1.00$, plotted for a range of compressibility percentages in the initial conditions - □: 100% dilatational; △: 70% dilatational; ×: 30% dilatational; ○: 0% dilatational. Figures represent (a) b_{11}^s, (b) b_{12}^s, (c) b_{22}^s and (d) b_{33}^s.

has the effect of isotropizing the flow (i.e. resisting the anisotropization of the flow by shear). The goal of this section is to see if similar observations may be made about the role of pressure-dilatation for an initially-dilatational field.

It is helpful to plot the non-zero components of the anisotropy tensor and observe the changes that occur as compressibility is increased in the initial conditions. The solenoidal and dilatational non-zero components of the anisotropy tensor for a representative case ($M_g = 1.00$) are plotted in Figs. 29 and 30, respectively.

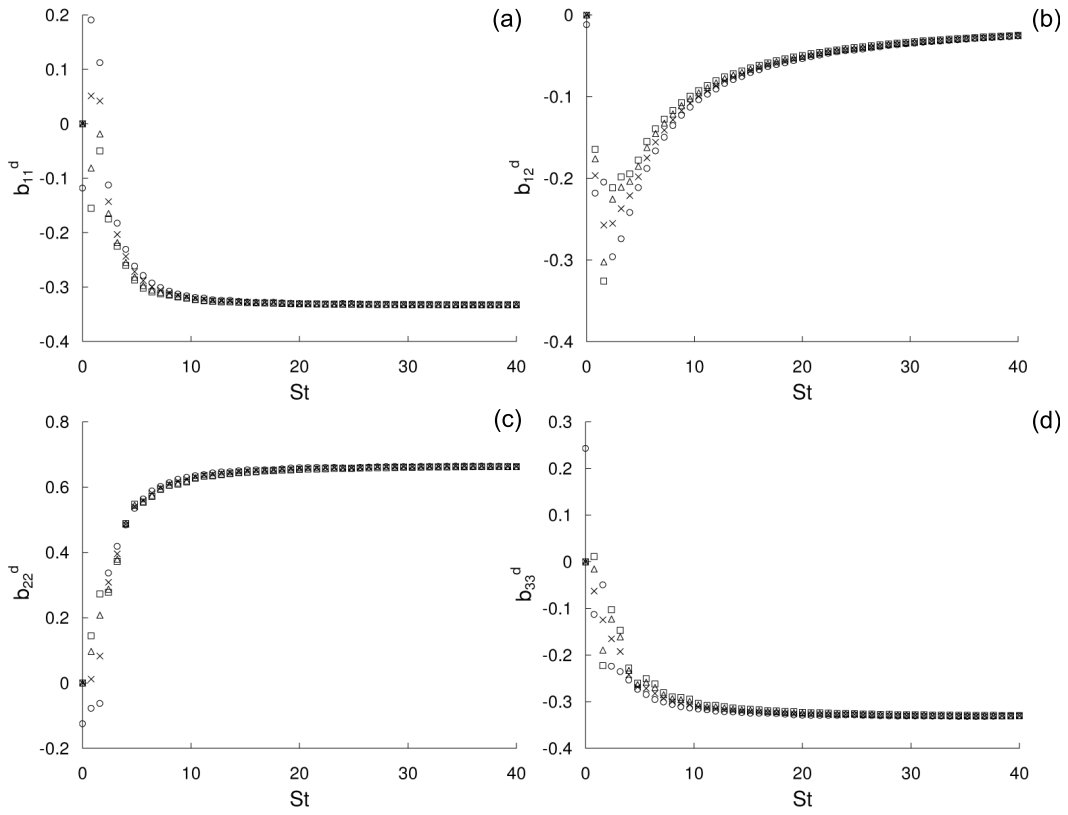

Fig. 30. Dilatational, non-zero components of the anisotropy tensor for $M_g = 1.00$, plotted for a range of compressibility percentages in the initial conditions - □: 100% dilatational; △: 70% dilatational; ×: 30% dilatational; ○: 0% dilatational. Figures represent (a) b_{11}^d, (b) b_{12}^d, (c) b_{22}^d and (d) b_{33}^d.

The solenoidal plots in Fig. 29 show fairly good agreement between the diagonal components, regardless of the initial amount of compressibility, once the flow has had time to develop. Only for the b_{12} component does the magnitude change significantly as compressibility is increased (except for the completely solenoidal case), indicating that solenoidal production grows with the amount of compressibility present in the initial field. The solenoidal anisotropy tensor components reveal that the flow becomes one-componential with all of the energy in the $\overline{u_1 u_1}$ component. The dilatational plots in Fig. 30 reveal good agreement between all compositions of the initial conditions. The flow reaches the anisotropic one-componential limit, this time with all of the energy contained in the $\overline{u_2 u_2}$ term. Livescu & Madina [15] found a similar trend for inviscid and viscous RDT, as well as for DNS: the dilatational velocity field moves to the one-componential limit as a result of the (2,2) component of the dilatational kinetic energy.

For the sake of comparison, the solenoidal and dilatational anisotropies of a higher shear magnitude ($M_g = 28.8$) are plotted in Figs. 31 and 32, respectively. These figures show similar trends as with the $M_g = 1.00$ case, except that now all the solenoidal plots collapse onto one line. At distinct time intervals that double with each interval, there occurs distinct "kinks" in the evolution of the anisotropy tensor components. At these intervals, the steepness of the "kinks" in the plots increases as the amount of initial compressibility is increased. As these "kinks" move the flow away from anisotropy with increasing initial compressibility, they could be somehow related to pressure-dilatation (which also resists anisotropy). These sharp kinks occur at the same point in shear-time for all levels of M_g.

The conclusion that can be drawn from Figs. 29-32 is that the solenoidal component of the flow is largely unaffected by a change in initial compressibility (and, thus, an increase in the efficiency of $\langle pd \rangle$), while the dilatational component is affected

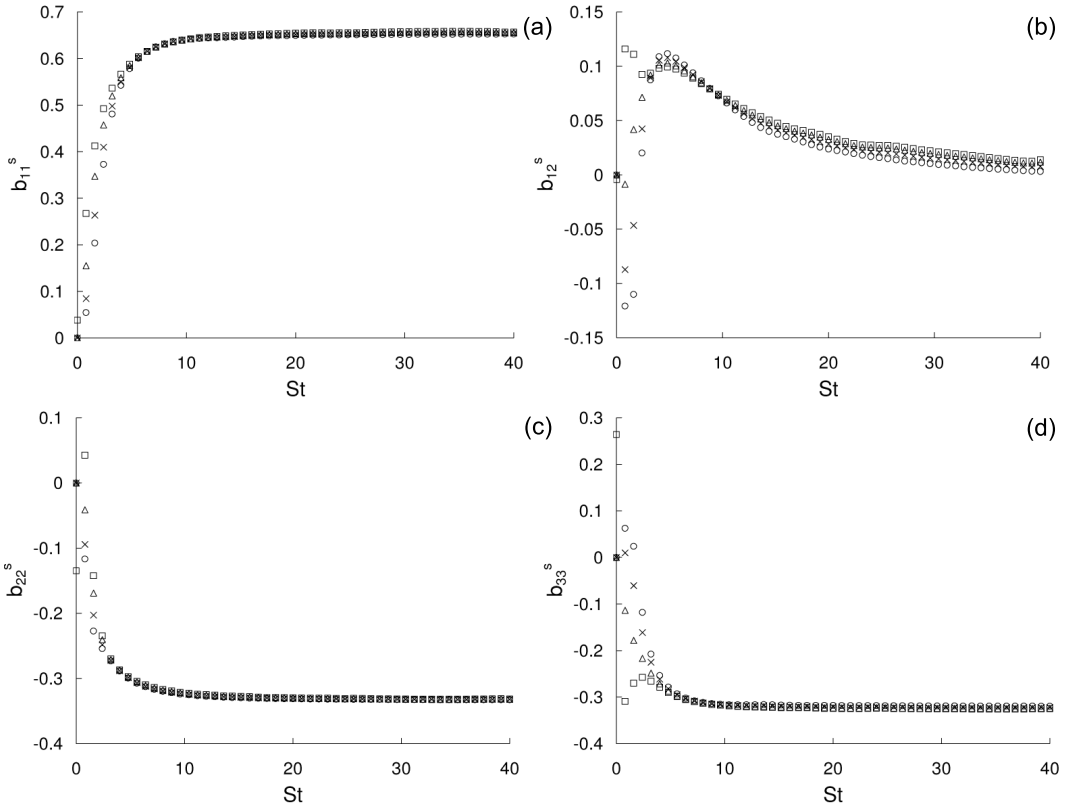

Fig. 31. Solenoidal, non-zero components of the anisotropy tensor for $M_g = 28.8$, plotted for a range of compressibility percentages in the initial conditions - □: 100% dilatational; △: 70% dilatational; ×: 30% dilatational; ○: 0% dilatational. Figures represent (a) b_{11}^s, (b) b_{12}^s, (c) b_{22}^s and (d) b_{33}^s.

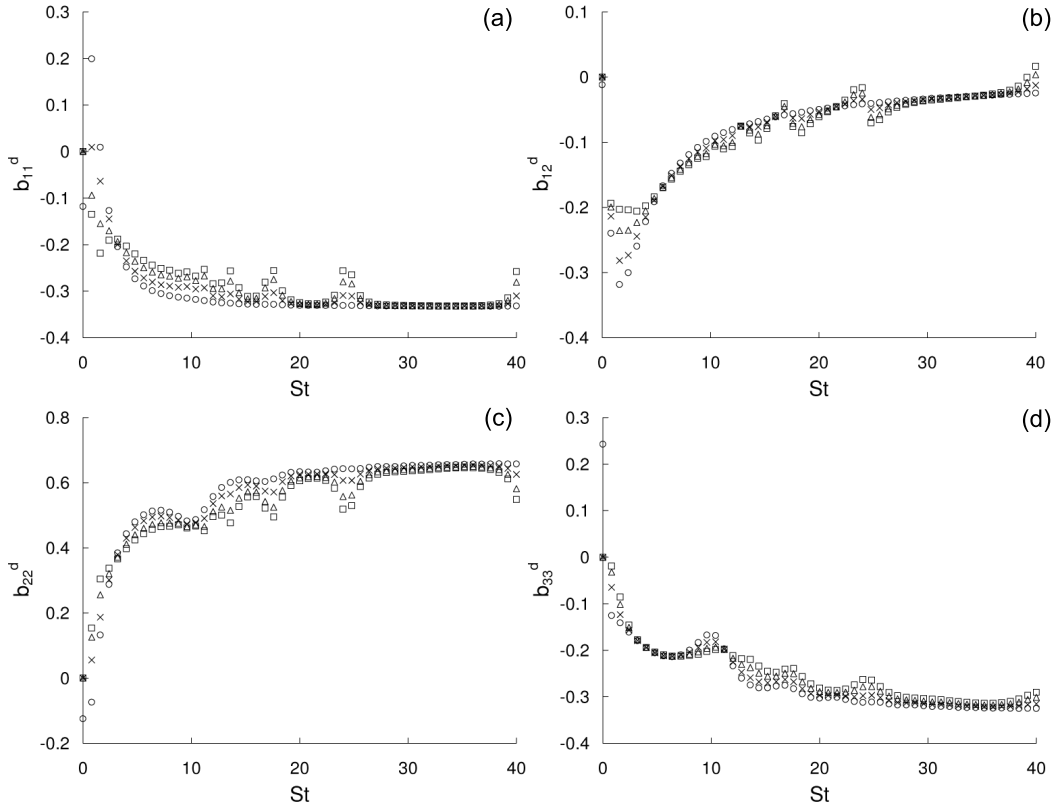

Fig. 32. Dilatational, non-zero components of the anisotropy tensor for $M_g = 28.8$, plotted for a range of compressibility percentages in the initial conditions - □: 100% dilatational; △: 70% dilatational; ×: 30% dilatational; ○: 0% dilatational. Figures represent (a) b_{11}^d, (b) b_{12}^d, (c) b_{22}^d and (d) b_{33}^d.

more and more at distinct intervals in shear-time as initial compressibility (and, thus, $\langle pd \rangle$ efficiency) is increased. Simone *et al.* [13] seem to draw the opposite conclusion, that being that compressibility has a greater effect on the solenoidal field than on the dilatational field; this conclusion is based upon observations of the evolution of the b_{12} component which, as can be seen in Figs. 29 and 30, holds true in R-RDT as the solenoidal b_{12} component experiences a greater change with increasing compressibility than does its dilatational counterpart. However, when examining all of the non-zero components of the anisotropy tensor, it is apparent that the Reynolds stresses which comprise the energy of the system seem to be less affected by compressibility in the solenoidal field than in the dilatational field.

E. Applicability of R-RDT

As has been noted, care must be taken in interpreting the R-RDT results and the degree of relevance to a given problem. Clearly, if one of the governing assumptions is violated, the above-mentioned results may not be valid. For example, if the applied shear is not very large, the R-RDT results may not be directly applicable. However, as applied shear increases, the R-RDT results will be more relevant.

We have noted the distinct regions in R-RDT and have stated that the physical time over which the shear-dominant and pressure-growth regions act is actually quite small. In fact, it is possible that such regions pass too rapidly to be detected in laboratory flows. However, these regions are useful in determining how rapid pressure influences turbulence and can be important in developing closure model criteria.

CHAPTER IV

RAPID DISTORTION THEORY: FAVRE-AVERAGED STATISTICS

In this section, we discuss salient features of the derivation of the Favre-averaged RDT equations (F-RDT), and briefly present the numerical implementation of the equations. Ultimately, the choice between the two methods depends upon the research goal. F-RDT provides statistics that are physically more meaningful, but at the expense of a more complicated mathematical formulation. On the other hand, the R-RDT formulation is simpler, but the quantities examined are of lesser physical relevance.

A. Methodology

The derivation of the F-RDT equations is similar to that of the R-RDT equations, with some important differences. While the main governing equations for F-RDT are the same, Favre decomposition is applied to velocity and temperature as:

$$U_i = \frac{\overline{\rho U_i}}{\overline{\rho}} + u_i^{"} = \tilde{U}_i + u_i^{"}, \tag{4.1a}$$

$$T = \frac{\overline{\rho T}}{\overline{\rho}} + T^{"} = \tilde{T} + T^{"}, \tag{4.1b}$$

respectively, while Reynolds decomposition is still applied to density. This approach yields the following mean field equations (linearized with the removal of second and higher-order terms as was performed with R-RDT):

$$\frac{\partial \overline{\rho}}{\partial t} + \frac{\partial (\overline{\rho} \tilde{U}_m)}{\partial x_m} = 0 \tag{4.2a}$$

$$\frac{\partial (\overline{\rho} \tilde{U}_i)}{\partial t} + \frac{\partial (\overline{\rho} \tilde{U}_i \tilde{U}_m)}{\partial x_m} = -R \frac{\partial (\overline{\rho} \tilde{T})}{\partial x_i} \tag{4.2b}$$

$$\frac{\partial \overline{\rho}\tilde{T}}{\partial t} + \frac{\partial \overline{\rho}\tilde{T}\tilde{U}_m}{\partial x_m} = -\frac{R\overline{\rho}\tilde{T}}{c_v}\frac{\partial \tilde{U}_m}{\partial x_m} \tag{4.2c}$$

When the mean field is subtracted from the linearized set of equations, the following four fluctuating equations are obtained:

$$\frac{d\rho^{'}}{dt} = -\frac{\partial \tilde{U}_m}{\partial x_m}\rho^{'} - \frac{\partial(\rho u_m^{"})}{\partial x_m} \tag{4.3a}$$

$$\frac{du_i^{"}}{dt} = -\frac{\rho^{'}}{\overline{\rho}}(\frac{d\tilde{U}_i}{dt} + R\frac{\partial \tilde{T}}{\partial x_i}) - u_m^{"}\frac{\partial \tilde{U}_i}{\partial x_m} - \frac{R}{\overline{\rho}}\frac{\partial(\rho T^{"})}{\partial x_i} - \frac{R\tilde{T}}{\overline{\rho}}\frac{\partial \rho^{'}}{\partial x_i} \tag{4.3b}$$

$$\frac{d(\rho u_i^{"})}{dt} = -\rho u_i^{"}\frac{\partial \tilde{U}_m}{\partial x_m} - \rho^{'}(\frac{d\tilde{U}_i}{dt} + R\frac{\partial \tilde{T}}{\partial x_i}) - \rho u_m^{"}\frac{\partial \tilde{U}_i}{\partial x_m} - R\frac{\partial(\rho T^{"})}{\partial x_i} - R\tilde{T}\frac{\partial \rho^{'}}{\partial x_i} \tag{4.3c}$$

$$\frac{d(\rho T^{"})}{dt} = -\rho T^{"}\frac{\partial \tilde{U}_m}{\partial x_m}(1 + \frac{R}{c_v}) - \rho u_m^{"}\frac{\partial \tilde{T}}{\partial x_m} - (\frac{d\tilde{T}}{dt} + \frac{R\tilde{T}}{c_v}\frac{\partial \tilde{U}_m}{\partial x_m})\rho^{'} - \frac{R\overline{\rho}\tilde{T}}{c_v}\frac{\partial u_m^{"}}{x_m} \tag{4.3d}$$

In this thesis, the homogeneity condition will also be applied in the F-RDT equations, allowing at this point the removal of spatial gradients of thermodynamic quantities. Using a similar Fourier approach as has already been described, the ODEs obtained are:

$$\frac{d\widehat{\rho}^{'}}{dt} = -i\kappa_m\widehat{\alpha}_m \tag{4.4a}$$

$$\frac{d\widehat{u}_i^{"}}{dt} = -\widehat{u}_m^{"}\frac{\partial \tilde{U}_i}{\partial x_m} - i\frac{R}{\overline{\rho}}\kappa_i(\widehat{\beta} + \tilde{T}\widehat{\rho}^{'}) \tag{4.4b}$$

$$\frac{d\widehat{\alpha}_i}{dt} = -\widehat{\alpha}_m\frac{\partial \tilde{U}_i}{\partial x_m} - iR\kappa_i(\widehat{\beta} + \tilde{T}\widehat{\rho}^{'}) \tag{4.4c}$$

$$\frac{d\widehat{\beta}}{dt} = -i(\gamma - 1)\overline{\rho}\tilde{T}\kappa_m\widehat{u}_m^{"} \tag{4.4d}$$

where:

$$\alpha_i = \rho u_i^{"}, \tag{4.5}$$

$$\beta = \rho T^{"}. \tag{4.6}$$

By constructing all possible fluctuating correlations of the above Fourier equations, one may obtain the following correlations:

$$\overline{u_i u_j} = \sum_{\vec{\kappa}} \widehat{A}_{ij}(\vec{\kappa}, t), \tag{4.7a}$$

$$\overline{\alpha_i \alpha_j} = \sum_{\vec{\kappa}} \widehat{B}_{ij}(\vec{\kappa}, t), \tag{4.7b}$$

$$\overline{\alpha_i u_j} = \sum_{\vec{\kappa}} \widehat{C}_{ij}(\vec{\kappa}, t), \tag{4.7c}$$

$$\overline{u_i \rho} = \sum_{\vec{\kappa}} \widehat{D}_i(\vec{\kappa}, t), \tag{4.7d}$$

$$\overline{\alpha_i \rho} = \sum_{\vec{\kappa}} \widehat{E}_i(\vec{\kappa}, t), \tag{4.7e}$$

$$\overline{u_i \beta} = \sum_{\vec{\kappa}} \widehat{F}_i(\vec{\kappa}, t), \tag{4.7f}$$

$$\overline{\alpha_i \beta} = \sum_{\vec{\kappa}} \widehat{G}_i(\vec{\kappa}, t), \tag{4.7g}$$

$$\overline{\beta \rho} = \sum_{\vec{\kappa}} \widehat{H}(\vec{\kappa}, t), \tag{4.7h}$$

$$\overline{\rho \rho} = \sum_{\vec{\kappa}} \widehat{I}(\vec{\kappa}, t), \tag{4.7i}$$

$$\overline{\beta \beta} = \sum_{\vec{\kappa}} \widehat{J}(\vec{\kappa}, t). \tag{4.7j}$$

where:

$$\widehat{A}_{ij} \equiv \langle \widehat{u}_i^* \widehat{u}_j | \vec{\kappa} \rangle, \tag{4.8a}$$

$$\widehat{B}_{ij} \equiv \langle \widehat{\alpha}_i^* \widehat{\alpha}_j | \vec{\kappa} \rangle, \tag{4.8b}$$

$$\widehat{C}_{ij} \equiv \langle \widehat{\alpha}_i^* \widehat{u}_j | \vec{\kappa} \rangle, \tag{4.8c}$$

$$\widehat{D}_i \equiv \langle \widehat{u}_i^* \widehat{\rho} | \vec{\kappa} \rangle, \tag{4.8d}$$

$$\widehat{E}_i \equiv \langle \widehat{\alpha}_i^* \widehat{\rho} | \vec{\kappa} \rangle, \tag{4.8e}$$

$$\widehat{F}_i \equiv \langle \widehat{u}_i^* \widehat{\beta} | \vec{\kappa} \rangle, \tag{4.8f}$$

$$\widehat{G}_i \equiv \langle \widehat{\alpha}_i^* \widehat{\beta} | \vec{\kappa} \rangle, \tag{4.8g}$$

$$\widehat{H} \equiv \langle \widehat{\beta}^* \widehat{\rho} | \vec{\kappa} \rangle, \tag{4.8h}$$

$$\widehat{I} \equiv \langle \widehat{\rho}^* \widehat{\rho} | \vec{\kappa} \rangle, \tag{4.8i}$$

$$\widehat{J} \equiv \langle \widehat{\beta}^* \widehat{\beta} | \vec{\kappa} \rangle, \tag{4.8j}$$

As mentioned before, it is more efficient to solve for the correlations directly. Therefore, constructing the evolution equations for the above correlations yields the following 64 ODEs:

$$\frac{dA_{ij}}{dt} = -A_{mj}\frac{\partial \tilde{U}_i}{\partial x_m} - A_{im}\frac{\partial \tilde{U}_j}{\partial x_m} + i\frac{R}{\overline{\rho}}\kappa_i(F_j^* + \tilde{T}D_j^*) - i\frac{R}{\overline{\rho}}\kappa_j(F_i + \tilde{T}D_i) \tag{4.9a}$$

$$\frac{dB_{ij}}{dt} = -B_{mj}\frac{\partial \tilde{U}_i}{\partial x_m} - B_{im}\frac{\partial \tilde{U}_j}{\partial x_m} + iR\kappa_i(G_j^* + \tilde{T}E_j^*) - iR\kappa_j(G_i + \tilde{T}E_i) \tag{4.9b}$$

$$\frac{dC_{ij}}{dt} = -C_{mj}\frac{\partial \tilde{U}_i}{\partial x_m} - C_{im}\frac{\partial \tilde{U}_j}{\partial x_m} + iR\kappa_i(F_j^* + \tilde{T}D_j^*) - i\frac{R}{\overline{\rho}}\kappa_j(G_i + \tilde{T}E_i) \tag{4.9c}$$

$$\frac{dD_i}{dt} = -D_m\frac{\partial \tilde{U}_i}{\partial x_m} + i\frac{R}{\overline{\rho}}\kappa_i(H + \tilde{T}I) - i\kappa_m C_{mi}^* \tag{4.9d}$$

$$\frac{dE_i}{dt} = -E_m\frac{\partial \tilde{U}_i}{\partial x_m} + iR\kappa_i(H + \tilde{T}I) - i\kappa_m B_{im} \tag{4.9e}$$

$$\frac{dF_i}{dt} = -F_m\frac{\partial \tilde{U}_i}{\partial x_m} + i\frac{R}{\overline{\rho}}\kappa_i(J + \tilde{T}H^*) - i(\gamma-1)\overline{\rho}\tilde{T}\kappa_m A_{im} \tag{4.9f}$$

$$\frac{dG_i}{dt} = -G_m\frac{\partial \tilde{U}_i}{\partial x_m} + iR\kappa_i(J + \tilde{T}H^*) - i(\gamma-1)\overline{\rho}\tilde{T}\kappa_m C_{im} \tag{4.9g}$$

$$\frac{dH}{dt} = i\kappa_m[(\gamma-1)\overline{\rho}\tilde{T}D_m - G_m^*] \tag{4.9h}$$

$$\frac{dI}{dt} = i\kappa_m(E_m - E_m^*) \tag{4.9i}$$

$$\frac{dJ}{dt} = i(\gamma-1)\overline{\rho}\tilde{T}\kappa_m(F_m - F_m^*) \tag{4.9j}$$

It is evident in these highly-coupled equations that the solution of all equations must be carried out to obtain a solution for the density-weighted turbulent kinetic energy. With these equations and the wavevector evolution equation in Eq. 2.19, one must solve 65 ordinary differential equations. Again, a fourth-order Runge-Kutta solver is used to solve for these equations.

B. Numerical Implementation

The numerical implementation for the Favre-averaged method is very similar to the R-RDT method. As mentioned, large homogeneous shear is imposed on a turbulence field that is initially incompressible and isotropic. The gradient Mach number M_g, as defined earlier, is used to control the inertia of the flow and allows for equal comparison between the two RDT methods. Density is also set so that $\overline{\rho} = 1.0$, while initial mean temperature is set to 300°K.

For the sake of comparison, the initial conditions for the velocity field in the R-RDT simulations (i.e. R_{ij}) are used in the F-RDT simulations (i.e. A_{ij}, B_{ij} and C_{ij}) as well. It is assumed that there are no fluctuations initially in the thermodynamic variables. Since mean density is set to unity and no fluctuations are specified in density, the result is that all initial velocity fields in the F-RDT equations exactly match the initial velocity field in the R-RDT equation. Steps are not taken to ensure the convergence of the F-RDT simulations, for reasons that will be discussed in detail in Chapter V.

CHAPTER V

F-RDT RESULTS

As mentioned in Chapter IV, significant examination of the Favre-averaged RDT equations is not performed for several reasons. The most readily-apparent reason is that identical plots are returned for the evolution of the kinetic (both density-weighted and non-density-weighted) and internal modes, as can be seen in Figs. 33, 34 and 35, respectively.

As can be seen when compared with the plots of initially-incompressible R-RDT kinetic energy and mean temperature evolution (Figs. 5 and 11, respectively), the F-RDT plots of kinetic energy and mean temperature are essentially the same for all values of M_g and time St.

The reason for the similarity between the two sets of results stems from the fact that the $\overline{\rho' u_i'}$ correlation in R-RDT is zero for all values of M_g at all times. By definition, the relation between the Reynolds-averaged mean velocity and the Favre-averaged mean velocity is as follows:

$$\tilde{U}_i = \frac{\overline{\rho U_i}}{\overline{\rho}} = \frac{1}{\overline{\rho}}\overline{(\overline{U_i} + u_i')(\overline{\rho} + \rho')} = \overline{U_i} + \frac{\overline{u_i'\rho'}}{\overline{\rho}} \tag{5.1}$$

Accordingly, if the correlation between fluctuating velocity and density (i.e. $\overline{\rho' u_i'}$) is zero, then the following is obtained:

$$\tilde{U}_i = \overline{U_i} \tag{5.2}$$

Returning to the definition of Reynolds and Favre decomposition for velocity, if Eq. (5.2) holds to be true, then:

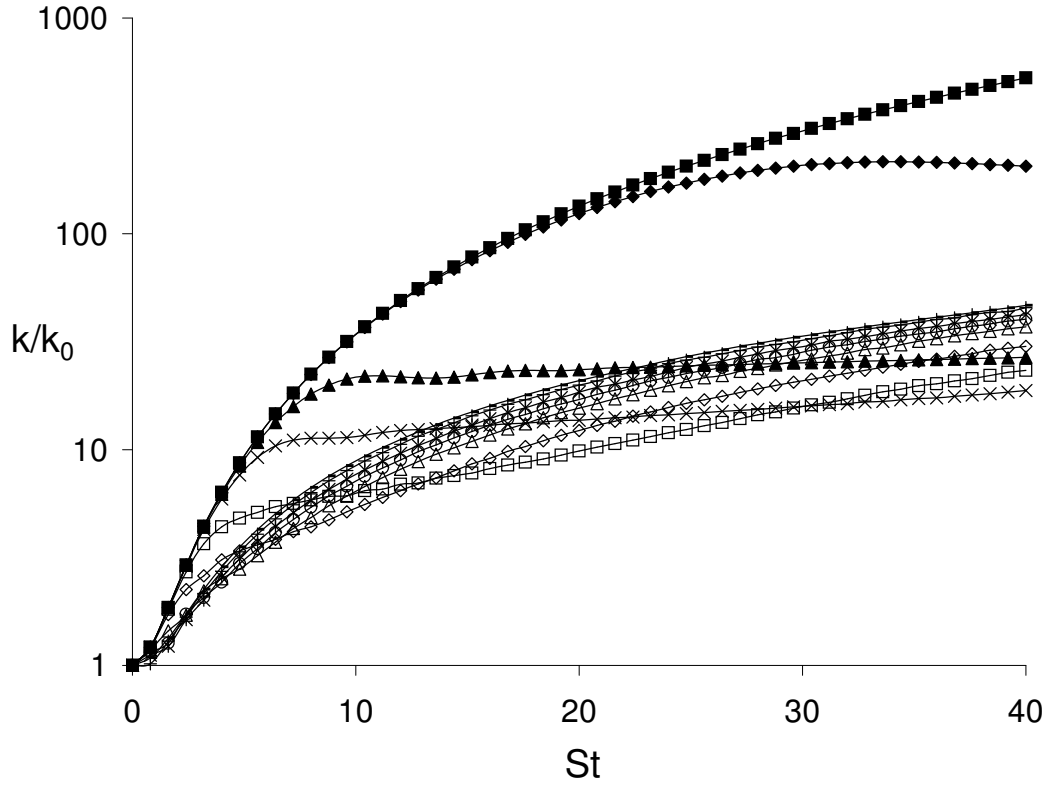

Fig. 33. The evolution of density-weighted normalized turbulent kinetic energy with solenoidal initial conditions from F-RDT simulations. Plotted for a range of gradient Mach numbers M_g: $-$: 0.01; $+$: 0.29; $*$: 0.72; $\circ$:1.00; $\triangle$: 1.44; $\Diamond$: 2.88; $\square$: 5.76; $\times$: 14.4; $\blacktriangle$: 28.8; $\blacklozenge$: 288; $\blacksquare$: 2880.

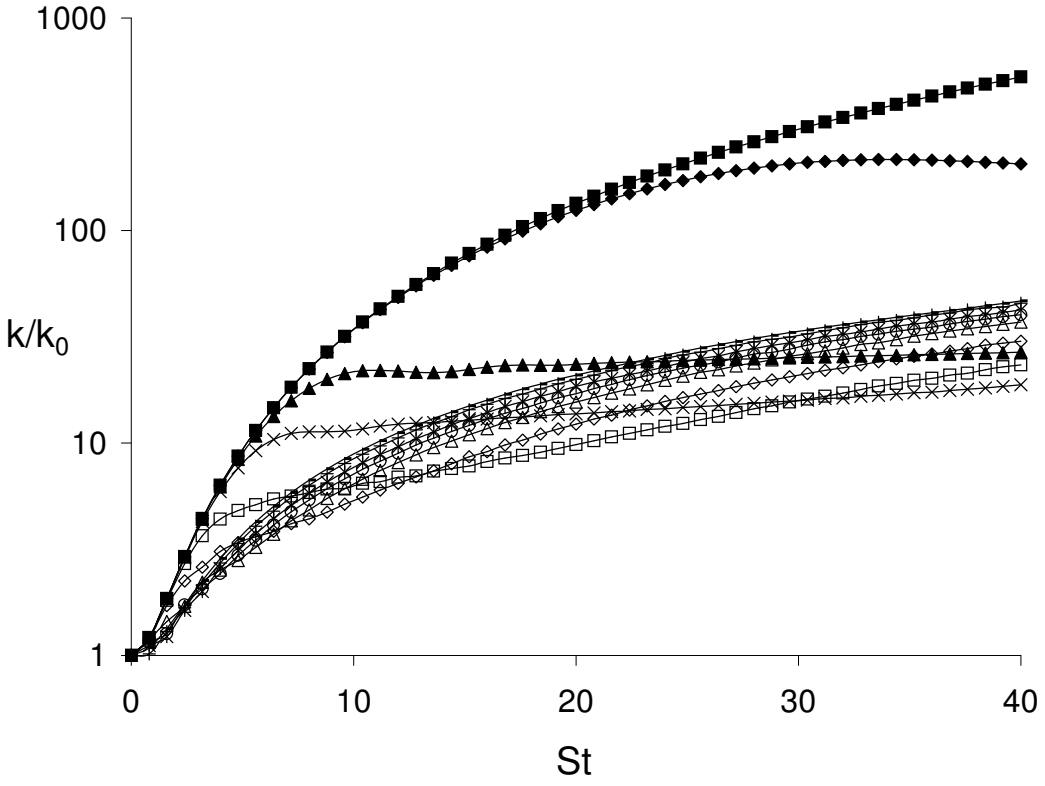

Fig. 34. The evolution of non-density-weighted normalized turbulent kinetic energy with solenoidal initial conditions from F-RDT simulations. Plotted for a range of gradient Mach numbers M_g: $-$: 0.01; $+$: 0.29; $*$: 0.72; $\circ$:1.00; $\triangle$: 1.44; $\Diamond$: 2.88; $\square$: 5.76; $\times$: 14.4; $\blacktriangle$: 28.8; $\blacklozenge$: 288; $\blacksquare$: 2880.

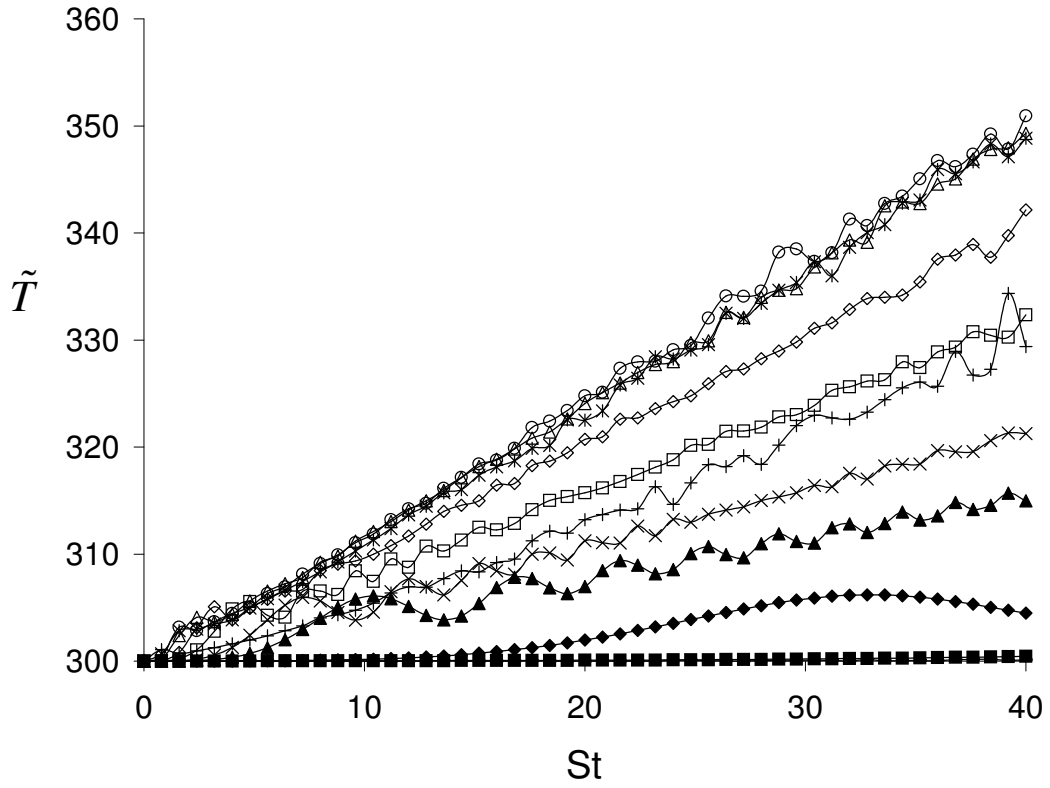

Fig. 35. Evolution of mean temperature for initially-solenoidal initial conditions from F-RDT simulations. Plotted for a range of gradient Mach numbers M_g: $-$: 0.01; $+$: 0.29; $*$: 0.72; $\circ$:1.00; $\triangle$: 1.44; $\Diamond$: 2.88; $\square$: 5.76; $\times$: 14.4; $\blacktriangle$: 28.8; $\blacklozenge$: 288; $\blacksquare$: 2880.

$$U_i = \tilde{U}_i + u_i^{"} = \overline{U_i} + u_i^{'} \tag{5.3}$$

$$\therefore u_i^{"} = u_i^{'} \tag{5.4}$$

Therefore, if the fluctuating velocities of both methods are the same, then the correlations of those fluctuating velocities (including the respective kinetic energies - $\overline{u_i u_i}$ - and work due to production - $\overline{u_1 u_2}$) will be the same, thereby leading to the same internal energy growth. This isn't necessarily true of the F-RDT method for all types of shear flows and has only been shown true in the case of homogeneous shear flow. Indeed, $\overline{\rho' u_i'}$ is expected to be more significant in the case of uniaxial compression shear flows (such as experienced across a shockwave); such types of flows require further study in the arena of F-RDT.

The R-RDT method is computationally easier to solve as compared to F-RDT (26 ODEs vs. 65 ODEs). For other mean shear flows where the two sets of data will differ, F-RDT ultimately will provide more meaningful physical results (such as density-weighted kinetic energy) and will likely be useful in future model development.

CHAPTER VI

CONCLUSIONS

Starting from first principles, a set of 26 ODEs that describe the evolution of compressible ideal gas turbulence in the rapid distortion limit are derived. The set includes equations for Reynolds-averaged first (mean) and second-order moments. Invoking the rapid distortion simplification allows all third-order moments to be taken as negligible. The corresponding fluctuation equations are linear and hence are easily amenable to solution techniques in Fourier space, a method routinely employed in incompressible rapid distortion theory (I-RDT). The validity of the compressible RDT equations and solution procedure has been established in concurrent work [14] by comparison against published incompressible RDT results [2] at one limit and analytical pressure-released Burgers turbulence at the infinite Mach number limit.

In this thesis, this validated and verified R-RDT method is applied to the problem of homogeneous shear turbulence subject to a range of gradient Mach numbers and initial compressibility. Further, the method is extended to Favre-averaged RDT (F-RDT), where equations are derived and preliminary validation has been completed. The main findings are now summarized.

A. Validation Against DNS

R-RDT analysis of initially-solenoidal turbulence is compared against direct numerical simulation (DNS) data [18] for interim gradient Mach numbers. Comparison is made for b_{12} anisotropy component (which is linked to production) and its solenoidal and dilatational parts, as well as with turbulent kinetic energy growth rate exponent Λ. Agreement in trends between the two sets of data as a function of gradient Mach number is good. The respective high-Mach number and incompressible limit results

match quite well. Similar agreement of previous RDT data with DNS data has been found in the past [13]. Mach number sensitivity at the asymptotic limit found in the DNS data is not obtained with R-RDT. Simone *et al.* [13] also observe this phenomenon and hypothesize that this loss of Mach-dependency is related to the neglecting of the higher-order nonlinear terms, as is common in general RDT.

B. Evolution of Kinetic Energy

The kinetic energy growth is initially more rapid than in incompressible RDT; however, at later times, the growth rate is slower. The solenoidal and dilatational components of kinetic energy and production present several interesting features: (i) at very low gradient Mach numbers (M_g), the initial composition of solenoidal to dilatational kinetic energy ratio (k_s/k_d) is preserved intact; (ii) at higher M_g for a given initial k_s/k_d, there is a tendency for the solenoidal fluctuations to dominate at later times; (iii) at a given M_g, asymptotic k_d/k_s increases with increasing initial k_d/k_s; (iv) maximum levels of k_d are observed for $M_g = 1.00$ for initially-solenoidal flows and (v) the M_g for which k_d is maximum decreases as initial compressibility increases.

C. Role of Pressure-Dilatation

Pressure-dilatation is responsible for the transfer of energy between the kinetic and internal modes. A study of pressure-dilatation magnitude reveals that it is at a maximum at approximately $M_g = 1.00$ for the initially-solenoidal case, and is lesser at higher and lower values of M_g. The amount of energy converted to the internal mode (and, thus, the influence of $\langle pd \rangle$) increases as the initial compressibility increases. Pressure-dilatation is negligible at the two extremes of M_g as there are negligible pressure effects at the Burgers limit and no dilatation present at the incompressible

limit.

D. Energy Balance of Kinetic and Internal Modes

At very high or very low M_g, there is very little increase in the amount of internal energy. At intermediate M_g, the internal energy growth rate approaches an asymptotic value at long values of St; that is, given enough time, the fraction of energy due to pressure work being transferred to the internal mode does not depend upon the gradient Mach number in the rapid-distortion limit. Oscillations present in the kinetic mode correspond with oscillations present in the internal mode, though exactly out of phase. Internal energy trends have similar tendencies as kinetic energy. The plots of internal energy initially follow the pressure-released Burgers curve, peel off in an oscillatory fashion, and approach a common, steady trend.

E. Three Distinct Regions of R-RDT

Compressible turbulence evolution in the rapid distortion limit is characterized by three regions: a shear dominant-region, a pressure "come-back" region and an asymptotic self-similar region where shear and pressure effects reach a balance and kinetic energy production appears to grow linearly. The relative sizes of these three regions are determined by M_g and the initial composition. These three regions are reflected in the b_{12} anisotropy component plot (which is an indicator of energy production): b_{12} initially follows the Burgers trend, peels off in an oscillatory manner approaching zero (explaining why plots of kinetic energy for some gradient Mach numbers are relatively flat in this region) and then settles to a small, but constant, negative value. Due to this negative b_{12}, kinetic energy grows slowly in the asymptotic state.

F. Effect of Initial Dilatation

Increasing the initial amount of compressibility is found to have several effects on the flow. It has already been stated that the influence of pressure-dilatation increases with initial compressibility. Kinetic energy evolution is slower than in the initially-solenoidal case, but internal energy grows more rapidly. Similarly, the internal energy growth at long St is much higher for the initially-compressible case as compared to the initially-incompressible case. Increased initial compressibility also leads to an initial decrease in kinetic energy for $M_g \leq 1.44$, as kinetic energy is transferred to the internal mode before significant production occurs.

G. Compressibility Effects on Anisotropy

While increasing initial compressibility enhances the effectiveness of pressure-dilatation and affects the dilatational components of the anisotropy tensor, it leaves the solenoidal component mostly unchanged. Examining the solenoidal and dilatational components of anisotropy reveals that the streamwise component - i.e. (1,1) - is dominant in the solenoidal portion of the flow while the stream-normal component - i.e. (2,2) - is dominant in the dilatational portion of the flow.

H. R-RDT vs. F-RDT Comparison

For the case of homogeneous shear flow, no significant difference is found in the results from the R-RDT and F-RDT simulations. This is due to the fact that the density-velocity fluctuation correlation (i.e. $\overline{\rho' u'}$) is zero for all times at all gradient Mach numbers. However, this may not indicate that F-RDT will be identical to R-RDT for other types of mean deformation.

This work was supported by AFOSR (MURI) Grant No. FA9550-04-1-0425 (Pro-

gram Manager: Dr. John Schmisseur) and by the National Defense Science and Engineering Graduate (NDSEG) Fellowship through the High Performance Computing agency with the Department of Defense.

REFERENCES

[1] G. K. Batchelor and I. Proudman. "The effect of rapid distortion of a fluid in turbulent motion." *Q. J. Mech. Appl. Math.*, 7:121–152, 1954.

[2] B. S. Pope. *Turbulent flows.* Cambridge University Press, 2000.

[3] A. M. Savill. "Recent developments in rapid distortion theory." *Ann. Rev. Fluid Mech.*, 19:531–573, 1987.

[4] J. C. R. Hunt and D. J. Carruthers. "Rapid distortion theory and the 'problems' of turbulence." *J. Fluid Mech.*, 212:497–532, 1990.

[5] C. Cambon, G. N. Coleman, and D. N. N. Mansour. "Rapid distortion analysis and direct simulation of compressible homogeneous turbulence at finite Mach number." *J. Fluid Mech.*, 257:641–665, 1993.

[6] G. Brethouwer. "The effect of rotation on rapidly sheared homogeneous turbulence and passive scalar transport; linear theory and direct numerical simulations." *J. Fluid Mech.*, 542:305–342, 2005.

[7] S. S. Girimaji, J. R. O'Neil, and D. Yu. "Rapid distortion analysis of homogeneous turbulence subjected to rotating shear." *Phys. Fluids*, 18, 2006.

[8] P. A. Durbin and O. Zeman. "Rapid distortion theory for homogeneous compressed turbulence with application to modelling." *J. Fluid Mech.*, 242:349–370, 1992.

[9] G. A. Blaisdell, G. N. Coleman, and N. N. Mansour. "Rapid distortion theory for compressible homogeneous turbulence under isotropic mean strain." *Phys. Fluids*, 8:2692–2705, 1996.

[10] G. N. Coleman and N. N. Mansour. "Modeling the rapid spherical compression of isotropic turbulence." *Phys. Fluids A*, 3:2255–, 1991.

[11] G. N. Coleman and N. N. Mansour. "Simulation and modeling of homogeneous compressible turbulence under isotropic mean compression," in *Turbulent Shear Flows 8*, pages 269–282, Berlin: Springer-Verlag, 1993.

[12] L. Jacquin, C. Cambon, and E. Blin. "Turbulence amplification by a shock wave and rapid distortion theory." *Phys. Fluids A*, 5:2539, 1993.

[13] A. Simone, G. N. Coleman, and C. Cambon. "The effect of compressibility on turbulent shear flow: a rapid-distortion-theory and direct-numerical-simulation study." *J. Fluid Mech.*, 330:307–338, 1997.

[14] H. Yu and S. S. Girimaji. "Extension of compressible ideal-gas RDT to general mean velocity gradients." Accepted for publication in *Phys. Fluids*, 2007.

[15] D. Livescu and C. K. Madnia. "Small scale structure of homogeneous turbulent shear flow." *Phys. Fluids*, 16:2864–2876, 2004.

[16] S. C. Kassinos and W. C. Reynolds. "A particle representation model for the deformation of homogeneous turbulence." *Annual Research Briefs,* Center for Turbulence Research, NASA Ames/Stanford University, pages 31–53, 1996.

[17] S. S. Girimaji, E. Jeong, and S. V. Poroseva. "Pressure-strain correlation in homogeneous anisotropic turbulence subject to rapid strain-dominated distortion." *Phys. Fluids*, 15:3209–3222, 2003.

[18] S. Sarkar. "The stabilizing effect of compressibility in turbulent shear flow." *J. Fluid Mech.*, 282:163–186, 1995.

VITA

Tucker Alan Lavin received his Bachelor of Science degree in Aerospace Engineering from Texas A&M University in 2003. After a brief stint in industry, he returned to Texas A&M to receive his Master of Science degree in May 2007. His research interests include CFD of turbulent jet wakes and turbulence modeling in the linear regime. His publications include *Investigation of Turbulent Square Jet Using PANS Method* (44th AIAA Aerospace Sciences Mtg.) and *Reynolds-Averaged Rapid Distortion Analysis of Compressible Ideal-Gas Shear Turbulence* (under consideration for publication in J. Fluid Mech.).

He can be reached at Texas A&M University, Department of Aerospace Engineering, TAMU 3141, College Station, TX 77843-3141. He can be reached by e-mail at tucker@tamu.edu.